Nanoscale

REVIEW

View Article Online
View Journal | View Issue

Cite this: *Nanoscale*, 2025, **17**, 8975

Recent advances in 2D MXene-based heterostructures for gas sensing: mechanisms and applications in environmental and biomedical fields

Lanting Qian, *[a,b] Farnood Rahmati,*[c] Fengchao Li,[d] Tianzhu Zhang,[a] Tao Wang,[a] Haoze Zhang,[b] Shuo Yan[e] and Yun Zheng*[a]

MXenes, a unique class of 2D transition metal carbides, have gained attention for gas sensing applications due to their distinctive properties. Since the synthesis of $Ti_3C_2T_x$ MXene in 2011, significant progress has been made in using MXenes as chemiresistive sensors. Their layered structure, abundant surface groups, hydrophilicity, tunable conductivity, and excellent thermal properties make MXenes ideal for low-power, flexible, room temperature gas sensors, fostering scalable and reproducible applications in portable devices. This review evaluates the latest advancements in MXene-based gas sensors, beginning with an overview of the elemental compositions, structures, and typical fabrication process of MXenes. We subsequently examine their applications in gas sensing domains, evaluating the proposed mechanisms for detecting common volatile organic compounds such as acetone, formaldehyde, ethanol, ammonia, and nitrogen oxides. To set this apart from similar reviews, our focus centered on the mechanistic interactions between MXene sensing materials and analytes (particularly for chemiresistive gas sensors), leveraging the distinct functionalities of MXene chemistries, which can be finely tuned for specific applications. Ultimately, we examine the current limitations and prospective research avenues concerning the utilization of MXenes in environmental and biomedical applications.

Received 9th November 2024,
Accepted 5th March 2025

DOI: 10.1039/d4nr04681a

rsc.li/nanoscale

1. Introduction

Gas sensors are critical in various applications, including disease diagnosis, environmental monitoring, public safety, and food quality evaluation.[1–3] Over the past five decades, numerous technologies have been developed for gas detection, encompassing conductometric, optical, electrochemical, thermoelectric, and acoustic sensors.[4–12] Among these, chemiresistive sensors are of particular interest due to their scalable production methods, low-cost, small footprint, and seamless integration with standard integrated circuit technologies.[13–15]

Since the 1960s, metal oxide semiconductors (MOS) have been extensively studied for their application in chemiresistive gas sensors. Their simple structure and high sensitivity to stimuli have positioned MOS-based materials in the ideal space for sensor integration. The gas-sensing properties of pristine MOS, corresponding heterostructures, surface modifications, and micro- and nanostructures have been thoroughly documented in various reviews and book chapters.[16–25] Consequently, MOS-based materials have been successfully commercialized and deployed in many fields ranging from industrial and agriculture to pharmaceutical applications.[26–30] Despite the advantages of MOS-based gas sensors, several practical constraints and unresolved challenges impede their further advancement. A primary concern is the requirement for high operating temperatures, typically 200–500 °C, to activate the adsorption of ionized chemical species necessary for detection reactions. Typically, this requirement translates to incorporating a heating element in the sensor device, limiting their potential application in many fields and low-power devices.[31–34] The high operating temperature of MOS-based sensors necessitates increased sensor design and fabrication complexity and diminished sensitivity due to thermally induced Ostwald ripening of nanoparticles.[35,36] Furthermore,

[a]*Institute of New Energy Materials and Engineering, College of Materials Science and Engineering, Fujian Engineering Research Center of High Energy Batteries and New Energy Equipment & Systems, Fuzhou University, Fuzhou 350108, P. R. China. E-mail: yunzheng@fzu.edu.cn*
[b]*Department of Chemical Engineering, University of Waterloo, Waterloo, ON N2L 3G1, Canada. E-mail: ltqian@uwaterloo.ca*
[c]*Department of Chemistry, University of Guelph, Guelph, ON N1G 2W1, Canada. E-mail: fpakrava@uguelph.ca*
[d]*Shandong Weifang Ecological Environment Monitoring Center, Weifang 261000, P. R. China*
[e]*Department of Materials and Engineering, University of Ottawa, ON K1N 6N5, Canada*

elevated temperature significantly limits these sensors' wide adoption and application, particularly in hazardous environments where flammable gases may ignite. In addition, MOS-based gas sensors face additional technical challenges, including baseline resistance drift, insufficient selectivity, and sensitivity to humidity, further limiting their use-case in many areas.[37–39]

To overcome these limitations described above, researchers have focused on exploring a wide range of material combinations and architectures, modifying sensing material surfaces, and scalable production methodologies. As a result, the critical metrics on assessment of a sensor device are often categorized into four key elements: sensitivity, selectivity, recovery time, and stability. Concurrently, there is a growing emphasis on detecting gas molecules at or near room temperature to usher in a new wave of sensing devices that are compatible with the current surge in consumer electronics.[40–43] The rapid growth of the Internet of Things (IoT) and flexible electronics has driven a heightened demand for gas sensors that are flexible, wearable, energy-efficient, and compact.[26] Further, advancements in nanotechnology have stimulated interest in gas-sensing technologies that focus on device miniaturization and enhanced sensing performance through the application of innovative low-dimensional materials.[44–46] Recently, emerging 2D materials have attracted significant interest for the development of room temperature chemiresistive gas sensors, thanks to their high surface-to-volume ratio and exceptional physicochemical properties. The introduction of graphene-based gas sensors spurred exploration into a broader range of 2D materials for room temperature gas sensing applications.[47–52] Since 2011, MXenes—a subset of 2D materials including transition metal carbides, nitrides, carbonitrides, and oxycarbides—have gained considerable attention due to their unique surface chemistry, tunable interlayer spacing,[53,54] and diverse physicochemical properties.[55–57]

The MXene family consists of a wide variety of materials based on composition and structure, such as single transition metal MXenes, ordered phases, and high-entropy (h) MXenes.[58–67] Recent research[58,68–71] has shown that MXene-based materials offer excellent gas sensing performance at room temperature, capable of detecting ultra-low gas concentrations due to their high signal-to-noise ratio. However, pristine MXene-based gas sensors face challenges, including low sensitivity, baseline drift, susceptibility to cross-interference, and a narrow band gap, which limits surface reactions and sensor responsiveness. Additionally, MXenes' tendency to self-stack hinders gas diffusion and access to active sites, further restricting their ability to detect low-concentration gases.[72] While pristine MXenes offer a promising foundation for developing selective and sensitive room temperature gas sensors, further research is needed to better understand the gas sensing mechanisms and to scale up production of MXene-based sensors. Overcoming these challenges, such as improving response, selectivity, detection limits, and reversibility, is essential for unlocking the full potential of MXene-based materials in advanced gas sensing technologies.

In this review, we explored recent advancements in 2D MXene-based heterostructures, focusing specifically on gas sensing mechanisms (particularly for chemiresistive gas sensors) within environmental and biomedical applications. Unlike other studies, we emphasized the unique mechanistic interactions between MXenes and analytes, enabled by the tunable chemistries of MXenes, which facilitate enhanced sensitivity and selectivity for various gases. Our comprehensive analysis includes the distinct functionalities and room temperature capabilities of MXenes, making them viable for low-power, scalable gas-sensing applications. By addressing existing limitations and proposing future research avenues, this review serves as a valuable resource for researchers, academics, and industry professionals aiming to push the boundaries of MXene-based sensing technologies. We believe this work will contribute to advancing the integration of MXenes into next generation sensor technologies, aligning with the growing demands of environmental and health monitoring.

2. 2D materials for gas sensing

In 2011, the landscape of 2D materials was predominantly composed of semiconductors, semimetals, and insulators characterized by low electronic conductivities and carrier concentrations. At that time, few 2D materials could be produced in quantities sufficient for applications beyond microelectronics. Solution-processed 2D materials, with the exceptions of graphene and hexagonal boron nitrides, exhibited limited flake sizes due to low mechanical strength, which resulted in fracture during delamination. Many of these materials also demonstrated hydrophobic properties and instability in air.[73] The discovery of a family of 2D carbides and nitrides possessing metallic conductivity, hydrophilicity, processing ease, high yields, and large flakes subsequently transformed the materials science field.[74] Early transition metal carbides and nitrides had established themselves as an important material class, distinguished by their high metallic electrical conductivity, exceptional hardness, and superior chemical stability. These materials had been extensively studied for decades as bulk ceramic materials, primarily for high-temperature applications and cutting tools. Their applications extended to functional composites, catalysts, and electrochemical energy storage.

The strong bonding between transition metal and carbon/nitrogen atoms, predominantly through covalent and metallic bonds,[75] had previously made dimensionality reduction—from bulk 3D solids to nanomaterials including 2D sheets and 1D nanoribbons or nanotubes—particularly challenging. This necessitated unconventional approaches to achieve dimensionality reduction, and as a result, Gogotsi and coworkers developed an approach that utilized the difference in strength between metal–metal bonds and metal–carbon/nitrogen bonds to selectively etch monoatomic metal layers from the MAX

phases. These MAX phases were layered ternary carbides and nitrides with a composition of $M_{n+1}AX_n$, where M represented an early transition metal, A primarily comprised group 13 and 14 elements, X denoted carbon and/or nitrogen, and n ranged from 1 to 4. In 1996, Barsoum and El-Raghy achieved a breakthrough by producing single-phase pure samples of Ti_3SiC_2, demonstrating its machinability and excellent electrical and thermal conductivity.[76] By 1997, they had established that Ti_3SiC_2 was one of 50 phases, most of 2011 which had been discovered by Nowotny and colleagues in the 1960s.[77,78] The discovery of Ti_4AlN_3 in 1999 led to the designation of these materials as $M_{n+1}AX_n$ or MAX phases.[79]

Structurally, the MAX phases exhibited layered hexagonal characteristics (*P*63/*mmc* space group) and could be described as transition metal carbide/nitride sheets of octahedral blocks, with X atoms positioned in the octahedron centers, connected by pure A layers.[80] In 2011, Naguib and coworkers demonstrated that immersing Ti_3AlC_2 in hydrofluoric acid at room temperature enabled selective etching of the Al layers, resulting in the first 2D titanium carbide—Ti_3C_2.[81] By 2012,[82] this selective etching method had been shown to apply to numerous other MAX phases containing aluminum A-layers, one of the more common A-elements in MAX phases. This development led to the designation of this new family as MXenes, emphasizing their relationship to MAX phases and their dimensionality. While approximately 70 MAX phases existed in 2011,[83] by the time of documentation, the number had grown to 150, with new discoveries occurring regularly, providing an expanding array of precursors for MXenes. The critical performance metrics of gas sensor devices (sensitivity, selectivity, response and recovery time, detection limit, *etc.*) fundamentally depend on the characteristics of the sensing material utilized. Specifically, the large surface area of the sensing material facilitates the interaction between the material's active surface and the target gas molecules, while the availability of active surface sites enables efficient and selective adsorption of gas molecules.[84] In this context, two-dimensional nanostructures, which possess unique material properties that inherently differ from bulk structures, have garnered extensive research interest for development of high-performance gas sensors. In addition to providing an extensive surface area and thus increased active sites, 2D materials demonstrate several notable advantages, including facile surface functionalization, adjustable electronic structure, potential for 3D architectural assembly *via* stacking or sandwich-style approaches, superior flexibility enabling wearable use-cases enabling effective device integration compatibility, and exceptional mechanical durability.[85] As a result of implementation of 2D structures in this field, substantial improvements in the "4S" sensor performance parameters (sensitivity, selectivity, stability, and speed—response/recovery time) have been made in the past two decades.[86] For gas sensing applications, three primary categories of two-dimensional materials have emerged as the most extensively studied: (i) metal oxides,[87–90] (ii) graphene-based structures,[91–93] and (iii) dichalcogenides.[94–96] Metal oxide-based structures demonstrate exceptional sensitivity to gas molecules while maintaining robust stability.[97,98] These materials offer significant advantages in terms of cost-effective production and versatile manufacturing capabilities, enabling the creation of diverse nanostructured morphologies. The operational principle of metal oxide sensors relies on conductivity changes within the sensing surface layer, which vary according to environmental gas presence. The sensing mechanism progresses through distinct stages: initial adsorption of oxygen species on the semiconductor surface, electron transfer between semiconductor and oxygen, adsorption of the target gas, chemical reaction occurrence, electron transfer to the semiconductor, and finally, product desorption. The material's nanostructure and morphology play crucial roles in sensor performance. Specifically, porous structures facilitate enhanced surface-to-volume ratios, while large specific surface areas provide abundant active sites for gas molecule adsorption.[97,99] Graphene-based materials present compelling opportunities for gaseous molecule detection, primarily due to their exceptional electrical conductivity, remarkably high specific surface area, and superior charge carrier mobility.[99–101] These materials operate through a direct charge transfer mechanism, whereby the adsorption and desorption of gas molecules induce changes in local charge carrier concentration. The electrical conductivity undergoes either an increase or decrease, depending on whether the gas acts as an electron donor or acceptor.[102] Two-dimensional layered structures of transition metal dichalcogenides, notably MoS_2, $MoSe_2$, and WS_2 as frequently reported in literature, exhibit favorable semiconducting properties combined with high surface area and exceptional surface sensitivity. These characteristics have led to their widespread adoption in gas detection applications.[103,104] Their sensing mechanism closely parallels that of graphene-based materials, relying on charge transfer processes between the surface and adsorbed molecules.[105]

Beyond their general sensing capabilities, 2D materials provide an excellent foundation for developing gas sensors that operate effectively at low or room temperatures.[106] For example, Zhang and Yin successfully demonstrated high ethanol-sensing properties using SnO2 nanosheets at a relatively low operating temperature of 165 °C. The researchers attributed this exceptional sensor performance to the mesoporous texture of the nanosheets, combined with small grain sizes and surface defects, resulting in high response rates, rapid response/recovery times, and excellent selectivity.[107] While metal oxide-based gas sensors are able to function at low temperatures, graphene-based materials and transition metal dichalcogenides enable the development of room-temperature sensors.[108] The creation of graphene/CNT hybrid films and Pd-decorated graphene structures facilitates high-performance NO_2 detection at room temperature, presenting opportunities for low-power sensor device development.[109] Similarly, sensors utilizing WS_2 nanoflakes or WS_2 and MoS_2 thin films demonstrate significant potential for room-temperature ammonia detection, offering both high sensitivity and selectivity.[104,110] MXenes represent the next evolution of 2D

materials particularly suited for high-performance sensor development, further enabling low- and room-temperature applications with excellent sensitivity and response time. These materials possess exceptional electronic, physical, chemical, and mechanical properties, including large specific surface area, narrow and tunable bandgap, rapid electron transfer capability, and adjustable surface chemistry. While MXenes exhibit a 2D layered graphene-like morphology, they distinguish themselves from other 2D materials through superior response characteristics and enhanced signal-to-noise ratios, attributed to strong functional group binding with analytes. Their near-free electron states, positioned around the Fermi level, enable rapid charge-carrier transport through electron transport channels.[111–113] As a result, the superior sensing properties of MXenes stem primarily from their ability to effectively host a wide range of surface functional groups, which form strong bonds with analyte gases, and their metallic conductivity, facilitating rapid electron transfer and mobility.[114,115] The selectivity of MXene-based sensors depends significantly on several factors, including surface-gas molecule interactions, MXene compositions and charge states, and flake orientation. Additionally, their controllable surface terminations offer substantial opportunities for structural modification, leading to enhanced properties and improved sensing performance.[116]

3. 2D MXenes and MXene heterostructures

3.1 MAX and MXene structure

Since their discovery by Gogotsi *et al.* in 2011,[81] two-dimensional (2D) MXenes with nanosheet (NS) morphology have garnered significant interest due to their unique features, including their 2D structure, high conductance, tunable bandgap, excellent mechanical flexibility, and hydrophilicity. MXenes are derived from their precursor materials known as MAX phases, which have the formula $M_{n+1}AX_n$. In MAX phases, n ranges from 1 to 3, M is a transition metal, and A represents an element from groups 13–16 of the periodic table. Fig. 1 illustrates the elements involved in MAX phases and the corresponding MXenes, depicting a visual categorization of the precursor elements on the periodic table.[117] MXenes are characterized by the general formula $M_{n+1}X_nT_x$, where M represents a transition metal (*e.g.*, Mo, Ti, Zr, Cr), X denotes either carbon (C) or nitrogen (N), n ranges from 1 to 4, and T_x indicates surface termination groups (*e.g.*, –H, –O, –OH, –F). The atomic structure of MXenes consists of layers of M atoms arranged in a honeycomb-like 2D lattice, interspersed with X ions occupying the octahedral sites between adjacent metal layers, yielding highly ordered two-dimensional surfaces enabling a wide range of potential surface modifications.[118–120] Typically, the MXene structure is derived from separation of the MAX-phase precursor *via* selective etching and delamination in stages.[121,122] Fig. 1b and c [123,124] depicts a visual of the transition stages of Ti-based MAX phase, illustrating the inception of 2D layered MXene *via* typical HF etching and delamination synthesis route.

3.2 Synthesis of MXenes

3.2.1 HF etching. The first report on the synthesis of 2D Ti_3C_2 carbide, resulting from the selective removal of the Al atom layer from the Ti_3AlC_2 MAX-phase structure, was published in Gogotsi's pioneering work. This method demonstrated aluminum etching by HF acid, exploiting the different nature and strength of chemical bonds within the MAX-phase structure following the reaction (1), (2) and (3):[81]

$$M_{n+1}AlX_1 + 3HF = M_{n+1}X_n + AlF_3 + 1.5H_2 \quad (1)$$

$$M_{n+1}X_n + 2HF = M_{n+1}X_nF_2 + H_2 \quad (2)$$

$$M_{n+1}X_n + 2H_2O = M_{n+1}(OH)_2 + H_2 \quad (3)$$

The M–X (X = C, N) bonds in $M_{n+1}X_n$ layers are strong covalent-metal interactions, while the M–Al bonds are relatively weak metallic bonds, enabling selective bond cleaving *via* exposure to selective etchants. For MAX-phases containing more electronegative elements like Si instead of Al as the binding element, an additional oxidizing agent (*e.g.*, H_2O_2, $FeCl_3$, HNO_3, $NH_4S_2O_8$, $KMnO_4$) is often used alongside HF.[125,126]

However, the high toxicity and reactivity of hydrofluoric acid used in the etching process often result in defective MXenes and dramatic heating of the reaction system, leading to potential oxidation of the resulting MXenes.[127,128] To address these issues, a milder approach was developed using *in situ* generated HF through the interaction of HC acid with various metal fluorides (Li, Na, K, Fe). This method allows for better control of the synthesis process, producing less defective MXenes with fewer $M_{n+1}Xn$ layers.[68,129,130] The etchant composition significantly influences the surface functional groups (*e.g.*, –F,–OH, –O, –Cl) that form, which in turn affect the electrochemical properties of MXenes.

3.2.2 Delamination. Obtaining single or few-layered MXene plates using HF or HCl-MF etching systems (where M represents Li^+, Na^+, K^+, NH_4^+ cations) requires an additional delamination stage, often using intense ultrasound exposure or organic molecule intercalation. However, these processes can reduce the surface area and increase the defect rate. Alternative delamination methods have been recently explored, where $Ti_3C_2T_x$ MXenes are intercalated and exfoliated in polar organic molecules, followed by separation *via* mechanical vibration to obtain monolayers and few-layer $Ti_3C_2T_x$ MXenes. Alternatively, ultrasonication has been demonstrated to significantly boost high-quality nanosheet yield as well as process time, enabling a scalable pathway towards large-volume production. Furthermore, Dimethyl sulfoxide (DMSO) or tetrabutylammonium hydroxide (TBAOH) have been reported to be effective followed by manual shaking to obtain freestanding MXene "paper", eliminating energy-intensive sonication processes in MXene production.[68,131,132]

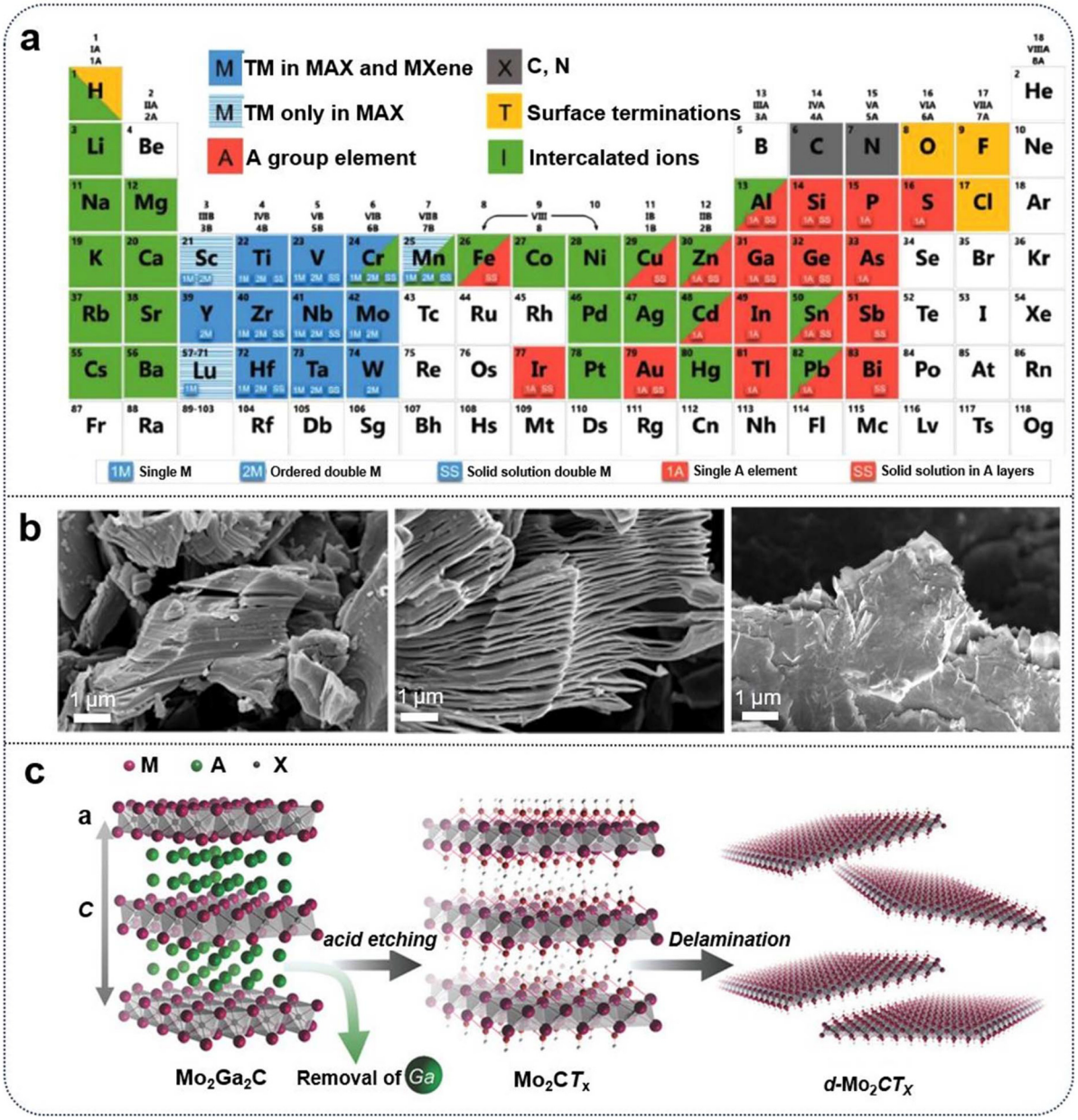

Fig. 1 (a) Periodic table displaying elements in MAX phases and MXenes, including surface terminations and intercalant cations derived from experimental investigations.[74] (b) left to right: SEM images of Ti_3AlC_2 MAX powder, multilayered $Ti_3C_2T_x$ MXene powder synthesized using 30 wt% HF, single MXene sheet post delamination.[80] (c) Schematic demonstrating Mo_2Ga_2C MAX and MXene structures.[81]

While these delamination strategies demonstrate notable improvements in yield from the original synthesis methodology, a scalable method to synthesize large defect-free MXenes is highly sought after to enable large-volume production. In this effort, to obtain large, non-defective $Ti_3C_2T_x$ particles, the Minimally Intensive Layer Delamination (MILD) technique was developed, optimizing the interaction between the Ti_3AlC_2 MAX-phase and the HCl-LiF system.[121,123] This method employs higher $n(\mathrm{LiF}):n(\mathrm{M}_{n+1}\mathrm{AlX}_n)$ and $n(\mathrm{HCl}):n(\mathrm{LiF})$ ratios to facilitate aluminum layer etching and separate accordion-like MXene aggregates into individual plates without ultrasound, requiring only shaking. MXenes synthesized by the MILD method exhibit distinct morphology, aggregation patterns after drying, and mechanical and electrophysical properties compared to those produced by conventional etching methods using lithium fluoride solution in hydrochloric acid.

Reproducible and scalable MXene synthesis methodologies are still being developed to enable application in sensing devices. Given the similarities between MXenes and other 2D materials, many studies on MXene-based sensor device fabrication employ established methods like dip-coating or drop-coating to apply modified MXene structures for investigation

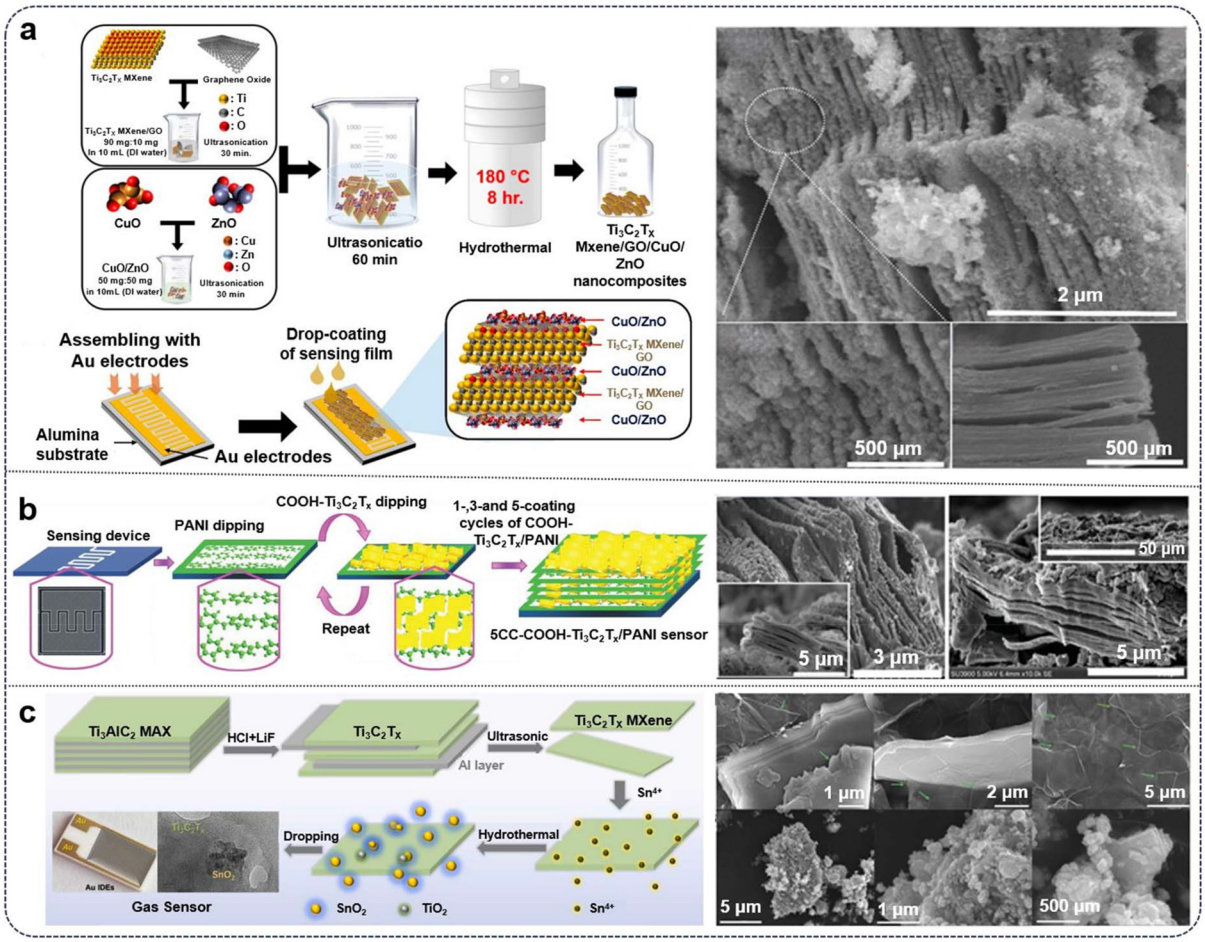

Fig. 2 (a) Synthesis schematic diagram of $Ti_3C_2T_x$ MXene/GO/CuO/ZnO nanocomposites.[90] (b) Schematic of sensor fabrication process using dip-method and coating cycles of COOH-$Ti_3C_2T_x$ /PANI.[91] (c) Illustration of preparation process of $Ti_3C_2T_x$-SnO_2 nanocomposite. The right side includes SEM images of the as-prepared MXene composites.[92]

of sensing properties [Fig. 2].[133–135] While the sensor device fabrication is crucial in demonstration of its commercial and scaling viability, device fabrication and integration will not be covered in the scope of this review.

The properties of synthesized MXenes exhibit significant variations depending on the chosen synthetic route, as these characteristics are fundamentally influenced by their surface functional groups, structural defects, and interlayer architectures. These two-dimensional materials demonstrate remarkable versatility, fulfilling the essential requirements for functional gas-sensing devices. The following discussion examines the latest reports on key intrinsic properties of MXenes that contribute to their gas-sensing capabilities, with particular emphasis on their structure–property relationships and sensing mechanisms.

4. Gas sensing principles

The sensing mechanism exhibited by MXene structures represents a distinct paradigm from that of metal oxides, demonstrating complexity that differs from the conventional surface adsorption or charge transfer mechanisms observed in traditional two-dimensional (2D) materials. While MOS-based sensors operate through well-established mechanisms involving interactions between gas molecules and pre-adsorbed oxygen species at the surface, MXenes exhibit fundamentally different sensing behavior.The intrinsic sensing mechanisms of both 2D MXenes and their heterostructures are central to their gas- sensing capabilities. Computational simulations have provided valuable insights into the gas-sensing mechanisms of pristine 2D MXenes. However, MXene heterostructures introduce additional complexity through their unique attributes, particularly in terms of their electronic structures and adsorption models, resulting in distinct sensing mechanisms.

4.1 Sensing mechanism of 2D MXenes

Since the initial discovery of MXenes, numerous MXene permutations have been reported,[57,67,69] with $Ti_3C_2T_x$ has emerged as the most extensively investigated member for gas

sensing applications. $Ti_3C_2T_x$ sensors exhibit behavior characteristic of p-type semiconductors, a phenomenon attributed to the presence of surface functional groups including –O, –OH, –F and *etc*. In gas sensing applications, charge carrier transfer is predominantly driven by physisorption and chemisorption. This attribute is influenced by the operating temperature, where at ambient temperatures, physisorption predominates such that a target gas molecule is absorbed onto the MXene surface without the mediation of adsorbed oxygen species. As a result, the measured electrical response of the system is changed *via* the process of adsorption and desorption, giving rise to gas detection mechanism.[136] This contrasts with MOS-based sensing mechanism, where adsorption of Oxygen on the surface is enabled at high temperature by capturing free electrons of the MOS, such that upon presence of a reducing gas, the surface density of adsorbed oxygen is changed thus allowing current flow, in accordance with its semiconductor properties. This fundamental difference in sensing mechanisms between MOS- and MXene-based gas sensors plays a crucial role in enabling ambient-temperature gas sensors, which are in high demand.

The electrical response is fundamentally determined by the chemical nature of the gas analytes, where reducing gases often induce an increase in electrical resistance, while the opposite is observed for oxidizing gases. This phenomenon is well-illustrated in Ti_3C_2 MXene interfaces with ammonia, where the generated electrons combine with holes in the MXene structure, resulting in a reduction in surface charge-carrier concentration and a corresponding increase in the resistance of $Ti_3C_2T_x$ sensors.[137,138] The p-type $Ti_3C_2T_x$ sensing reaction is demonstrated in eqn (4) and (5):

$$2NH_3 + 3O^- \rightarrow N_2 + 3H_2O + 3e^- \quad (4)$$

$$NH_3 + OH^- \rightarrow NH_2 + H_2O + e^- \quad (5)$$

MXene-based gas sensors generally operate at ambient temperature to avoid surface oxidation; therefore, the dominant adsorbed oxygen ions are typically of the O_2^- type. Upon introduction of an external gas, a reaction occurs between the adsorbed O_2^- ions and the gas, resulting in a change of MXene electrical conductivity. Further, in the case of a reducing gas, the interaction yields electrons, resulting in both hole formation and electron recombination, leading to an increase in MXene resistivity *via* hole depletion. Alternatively, when an oxidizing gas is encountered, electrons are consumed, leading to hole accumulation, decreasing resistivity.

4.2 Sensing mechanism of MXenes heterostructures

The gas sensing mechanism in MXene heterostructures is notably more complex due to the interplay between MXene and various materials, including metal oxides, polymers, and metal nanoparticles. These combinations result in diverse energy-band diagram configurations as these components interact with target molecules of either reducing or oxidizing gases. For instance, MXenes with p-type conductivity can be integrated with n-type or p-type semiconductors, forming p–p[139] or n–p[140] junctions based on the sensor device arrangement. Further additions of active materials to the MXene composites often adds another layer of complexity into the gas sensing process, where elucidation of fundamental sensing mechanisms aims to optimize the composition of the heterostructures. We chose Sn-based MXene composites as an example to discuss MXene heterostructure sensing mechanisms due to the consensus across many reports on their enhancing effect for MXenes.

Sn-based MXene composites stand out among MXene heterostructures owing to their low cost, non- toxicity, and availability.[140,141] A first report to the best of our knowledge, on SnO_2/MXene heterostructures capable of sensing NO_2 gas at ppb-level proposed the following mechanistic process. Given the *priori* on SnO_2 as a n-type semiconductor property with high electronegativity and intrinsic oxygen vacancies, a Schottky barrier is formed by addition of MXene, where due to a mismatch in Fermi level, electrons are injected from MXene to SnO_2 until system is equilibrated, leading to the band bending [Fig. 3a].[142] Further, introduction of target gases results affects the electron depletion layer (EDL), thus modulating electrical conductivity of the system.

Yu and coworkers used $Ti_3C_2T_x$-SnO_2, which was shown to have excellent NH_3 sensing response at room temperature due to the hybridization with SnO_2 *via* facile hydrothermal synthesis route.[143] Similarly, this work concluded the enhanced sensing property of the Sn-based MXene composite is due to the modulation of the depletion layer because of reactions between NH_3 molecule and the adsorbed oxygen ions [Fig. 3b]. Additionally, $Ti_3C_2T_x$ MXene functional groups provide favorable sites for gas adsorption, although an excessive amount of MXene can reduce response due to the blocking of active sites by numerous –OH termination groups.[143] In another study focused on SnO/MXene sensors for NH_3 detection, it was observed that when the $Ti_3C_2T_x$ MXene/SnO nanocomposite was exposed to ambient air at room temperature, adsorbed oxygen ions (O_2^-) contributed to the development of a thicker electron depletion layer, resulting in increased resistance. When the sensor was then exposed to ammonia vapor, NH_3 reacted with water molecules to produce NH_4^+, which subsequently underwent an oxidation reaction with the adsorbed oxygen O_2^-. This process released electrons back into the $Ti_3C_2T_x$ MXene/SnO sensing material. Electron transfer occurred from $Ti_3C_2T_x$ to SnO due to $Ti_3C_2T_x$ having a lower work function compared to SnO, causing band bending [Fig. 3c]. Essentially, the formation of a p–n junction enabled a greater return of electrons to the composite, thereby reducing the thickness of the electron depletion layer and resulting in lower resistance for the $Ti_3C_2T_x$ MXene/SnO nanocomposite in the presence of ammonia vapor. The authors remarked that the synergy between thin layer of SnO, high conductivity and specific area of $Ti_3C_2T_x$ MXene, along with the p–n junction forming between the two materials was the enabler for the high response and high selectivity of the sensor towards ammonia.[144]

Across the screened reports, the mono- and bi-metallic additions to MXene follows similar trends in terms of mechanistic processes of gas sensing, with many reported optimi-

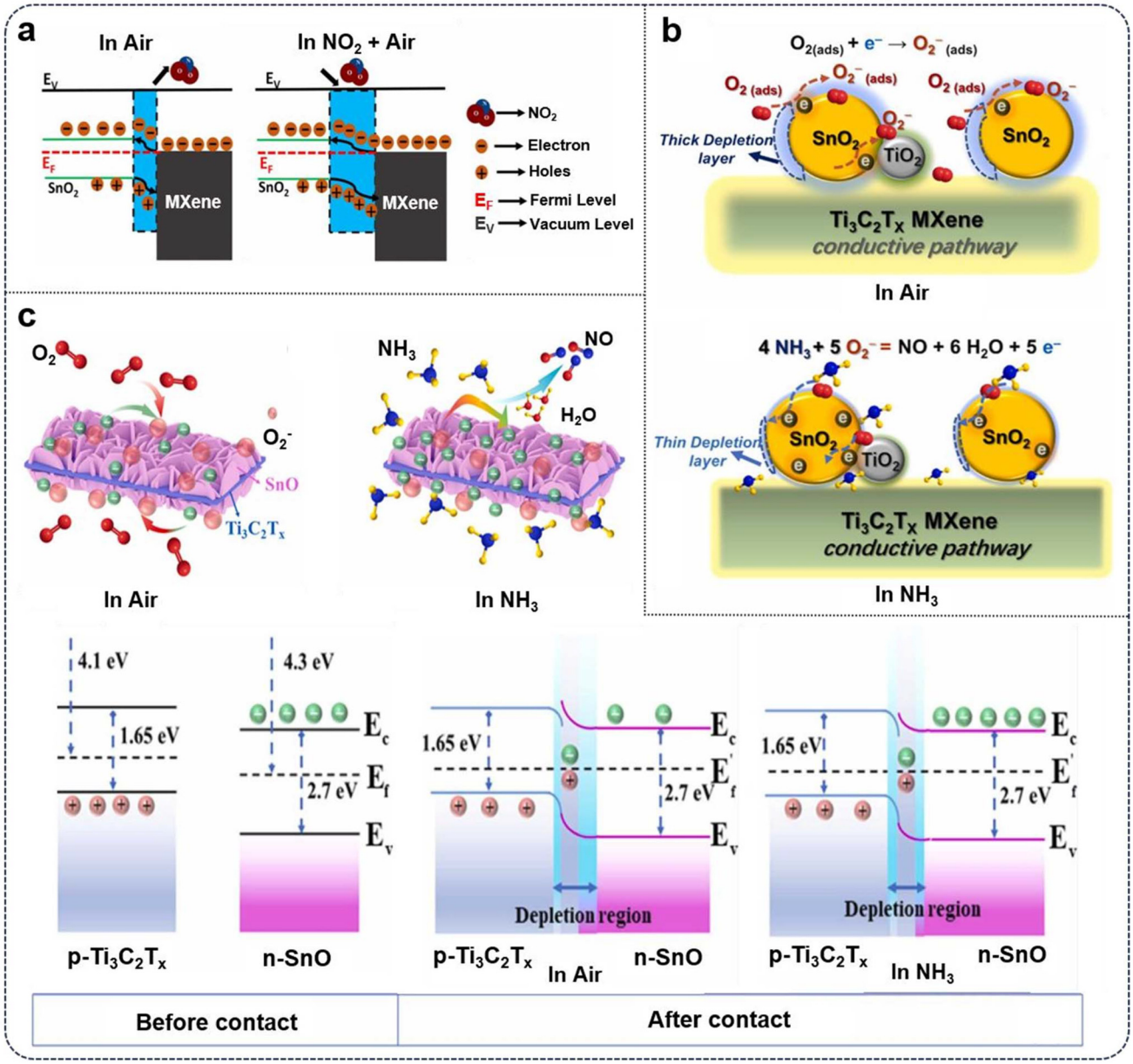

Fig. 3 (a) Sensing mechanism of SnO_2-MXene under air and NO_2 conditions.[99] (b) NH_3 sensing mechanism of $Ti_3C_2T_x$-SnO_2 composite sensor.[100] (c) Schematic of NH_3 sensing mechanism of $Ti_3C_2T_x$ MXene and SnO.[101]

zations in specific surface area and active site accessibly to enable maximum utilization of MXene framework as an ideal chemiresistive gas sensing device. We will dive further into MXene-based heterostructures modified for selective gas sensing towards common gases such as ammonia, and NO_2.

5. MXene-nanocomposites for gas sensing

5.1 Volatile organic compounds (VOC) gas sensors

The rapid pace of industrialization has led to higher emissions of toxic, flammable, and explosive gases, posing significant risks to both ecological systems and human health. Of special concern is acetone (CH_3COCH_3), a vital organic chemical extensively used in various industrial applications. However, despite its widespread utility, the flammable, explosive, and toxic nature of acetone imposes considerable threats to public safety and occupational health.[145–148] Prolonged exposure to acetone can result in severe health issues such as central nervous system depression, irritation of mucous membranes, ocular inflammation, and dizziness. At elevated concentrations, exposure could lead to unconsciousness, coma, or even death. Consequently, developing efficient methods for the rapid detection of acetone has become an urgent research priority. In this subsection, we briefly review a compilation of

recent reports on modified MXenes designed for selectivity towards VOCs, including acetone, ethanol, and formaldehyde. A recent report by Sun *et al.* demonstrated the utility of $ZnSnO_3$/ZnO nanofibers on a $Ti_3C_2T_x$ MXene sheet, whereby inclusion of the MXene component in the composite increased the sensor response value by a factor of 3.5, establishing a significant enhancement over the pristine nanofibers.[149] From an applied point of view, this enhancement in sensor sensitivity was observed in the optimum working temperature of the sensor where the highest response value is achieved, which was reported to be reduced from 200 °C to 120 °C. The synthesis of $ZnSnO_3$/ZnO/$Ti_3C_2T_x$ MXene composites was realized through a two-step process, initially creating $ZnSnO_3$/ZnO nanofibers *via* electrospinning, followed by their attachment to MXene sheets using a self-assembly method, which takes advantage of electrostatic interaction between the MXene and the nanofibers. In this composite architecture, $ZnSnO_3$/ZnO composite nanofibers acted as the active core material, while $Ti_3C_2T_x$ MXene nanosheets served as the conductive substrate. Furthermore, the composite structure established a p–n heterojunction between the n-type semiconductors (ZnO and $ZnSnO_3$) and the p-type $Ti_3C_2T_x$ MXene, facilitating enhanced electron transfer within the assembly, demonstrating the typical characteristic of n-type oxide-semiconductors. As a result, the three- dimensional composite structure, composed of $ZnSnO_3$/ZnO nanofibers distributed on 2D $Ti_3C_2T_x$ MXene nanosheets, was shown to synergistically accelerate electron transfer rates within gas-sensitive materials.

The synergies and heterostructures of $Ti_3C_2T_x$ MXene nanosheets with $ZnSnO_3$/ZnO in $ZnSnO_3$/ZnO/$Ti_3C_2T_x$ MXene composites were examined using a surface charge model, revealing intricate interactions between the components. With a band gap of 3.48 eV for $ZnSnO_3$/ZnO and the metallic nature of MXene—characterized by conduction and valence bands crossing the Fermi level—the composite displayed unique electronic properties. The difference in work functions between the MXene nanosheets (3.9 eV) and $ZnSnO_3$/ZnO (5.17 eV) triggered a charge transfer mechanism, where free electrons migrated from the MXene nanosheets to the $ZnSnO_3$/ZnO material. Fig. 4a visualizes this charge redistribution, which

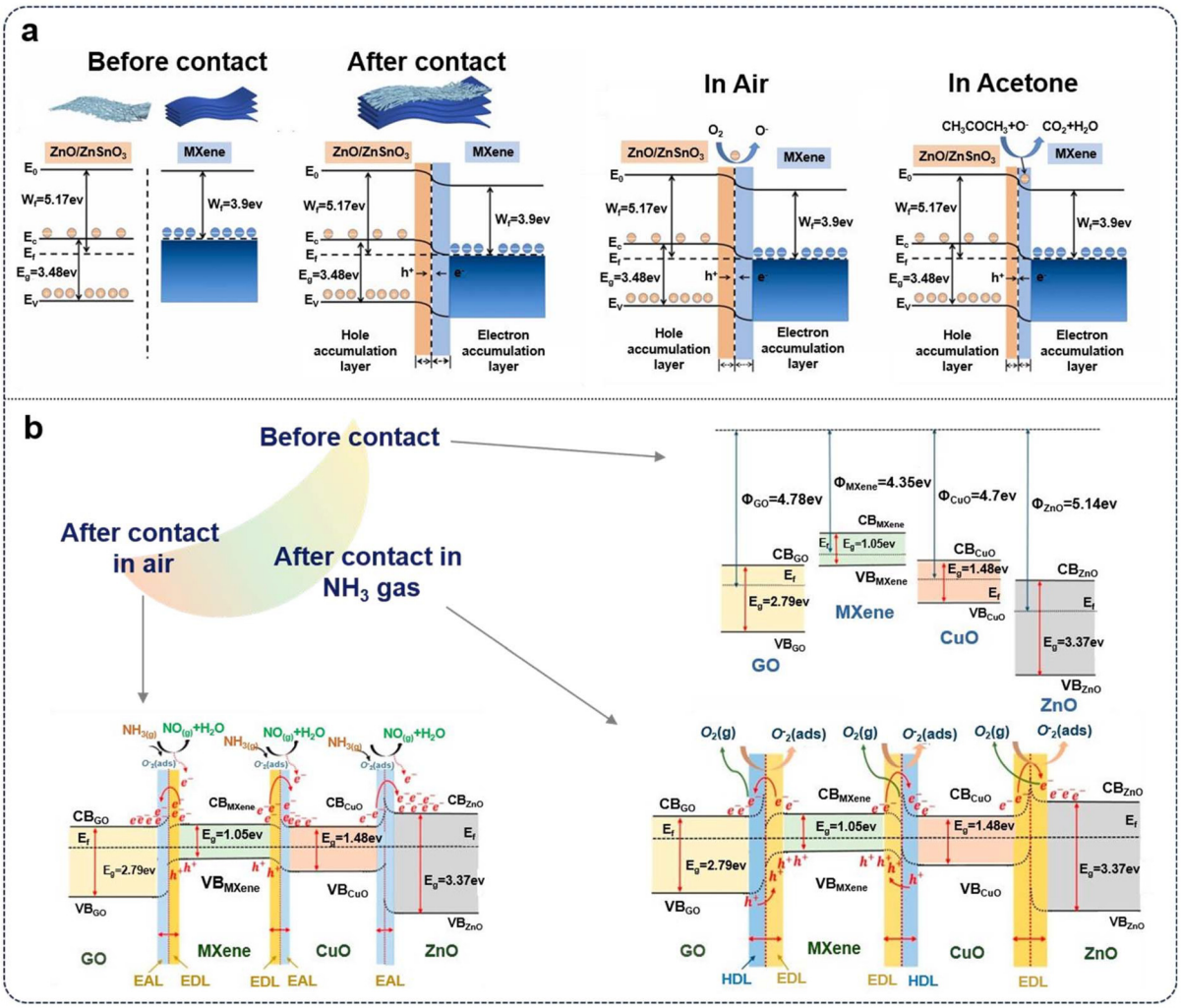

Fig. 4 (a) Illustration of gas sensing mechanism of $ZnSnO_3$/ZnO/$Ti_3C_2T_x$,[106] and (b) In O_2/ZnO_3/$Ti_3C_2T_x$ MXene composites.[111].

results in the formation of an electron depletion layer in the MXene nanosheets and an accumulation layer in the $ZnSnO_3$/ZnO material, consequently generating an internal electric field region akin to a barrier. This barrier ultimately impeded further electron transfer, facilitating the establishment of an equilibrium Fermi level within the $ZnSnO_3$/ZnO/$Ti_3C_2T_x$ MXene composite. Sun *et al.* further concluded that the enhancement of the $ZnSnO_3$ MOS perovskite sensing capability by incorporating MXene was proven to be a direct result of formation of heterojunctions with the MXene framework, thereby enabling a new paradigm of improvements to MOS-based sensors.

Considering the widespread use of VOCs in various industrial and consumer applications, researchers recognize their significant contribution to atmospheric pollution and potential for causing irreversible damage to human health.[150,151] Ethanol, a prominent VOC and important chemical raw material extensively utilized in food processing, medical treatment, and industrial production, garnered particular attention due to its pervasive presence and associated health risks. Prolonged exposure to ethanol gas was found to induce a range of adverse effects, including headaches, liver and kidney dysfunction, and paralysis of the central nervous system.[152,153] Consequently, the scientific community emphasized the critical importance of developing high-sensitivity monitoring systems for ethanol detection, aiming to mitigate its detrimental impact on environmental and human health.

In a study by Zhang *et al.*, metal–organic framework (MOF) derived In_2O_3/ZnO was synthesized with $Ti_3C_2T_x$ MXene to make a composite for detecting ethanol at room temperature, presenting a new strategy for room temperature gas sensing *via* utility of MOF and MXenes. They explored the mechanism of the MOF-MXene composite, finding that In_2O_3 and ZnO acted as n-type semiconductors, with In_2O_3/ZnO/$Ti_3C_2T_x$ MXene nanocomposites demonstrating n-type semiconductor characteristics.[154] Moreover, band structure analysis revealed that both the conduction band and valence band of $Ti_3C_2T_x$ MXene crossed the Fermi level, verifying its metallic properties and superior electrical conductivity [Fig. 4b]. Electrons were the primary charge carriers in the sensing process, thus, electron transfer occurred from In_2O_3 to ZnO, creating an n–n heterojunction at their interface. Similarly, electrons from $Ti_3C_2T_x$ MXene moved to In_2O_3, leading to band bending until reaching Fermi level equilibrium. In an air environment, O_2 captured electrons from ZnO, In_2O_3, and $Ti_3C_2T_x$ MXene to form oxygen ions (O_2^-). This process led to the formation of electron accumulation layers (EAL) and electron depletion layers (EDL) at the ZnO/In_2O_3 interface, while a hole accumulation layer (HAL) emerged at the In_2O_3/$Ti_3C_2T_x$ MXene junction. When ethanol gas was introduced, the molecules diffused and reacted with O_2^- ions on the In_2O_3/ZnO/$Ti_3C_2T_x$ MXene surface. As the reaction progressed, electrons released from the O_2^- ions combined with the holes in the HAL, reducing its thickness and increasing the Schottky barrier. Additionally, the formation of an n-n heterojunction reduced the thickness of the EDL and EAL, increasing electron concentration and decreasing the material's resistance.

Several factors were reported as critical contributors to the superior ethanol sensing capabilities of the In_2O_3/ZnO/$Ti_3C_2T_x$ MXene nanocomposites. First, the substantial specific surface area (48.9 $m2g^{-1}$) improved the adsorption of oxygen molecules and target gases, significantly enhancing sensor response. Secondly, $Ti_3C_2T_x$ MXene's rich functional groups (–O, –F, –OH) provided ample active sites for gas reactions. The inherent conductivity $Ti_3C_2T_x$ raised the carrier concentration in the material, thereby boosting ethanol sensing performance. Additionally, constructing the ternary In_2O_3/ZnO/$Ti_3C_2T_x$ MXene nanocomposite system markedly increased oxygen content (39.13%), further enhancing sensing efficiency. This report by Zhang and colleagues provides another excellent example of MXene derivatives that enable a significant boost to traditional sensing active materials that are hindered by low conductivity, selectivity, and poor stability. It is evident that incorporating MXene into traditional structures that excel at target gas adsorption can yield multiplicative and synergistic improvements without a significant synthesis or fabrication barrier, paving the way for applied and scaled-up solutions.

Detection of Formaldehyde (HCHO), a harmful indoor pollutant known to cause severe health issues, including respiratory system damage and cancer risk, has been a focus of investigation in the sensor research community.[155–157] Among various materials proposed for sub-ppm level formaldehyde detection in air, MOS-based materials, particularly SnO_2, had been extensively investigated[158–161] due to their fast response and low cost. While pristine $Ti_3C_2T_x$ MXene exhibited gas-sensing capability for NH_3, NO_2, and H_2, its performance is known to further improve when combined with metal oxide semiconductors like ZnO and CuO. However, premature oxidation of $Ti_3C_2T_x$ MXenes is a known failure mode wherein affecting the sensor's long-term stability when exposed to high humidity or high temperatures. It is well-documented that pristine MXene can exhibit instability due to the chemical oxidation of $Ti_3C_2T_x$ to TiO_2 in ambient environment, modulating sensor properties which lead to baseline shifts.[129–131] Given the importance of surface chemical states on gas sensing behaviour, the sensing performance of MXenes can be regulated through surface oxidations.

In a study conducted by Niu *et al.*,[162] the authors reported that TiO_2 generated through the synthesis process may form an n–n junction with SnO_2 nanosheets, which prior research indicated could improve the response to formaldehyde sensing. To tackle the stability issues associated with nanocomposites, they developed a hierarchical SnO_2/MXene nanocomposite using a simple one-step hydrothermal method. Additionally, to prevent uncontrolled oxidation of $Ti_3C_2T_x$ MXene, they implemented a strategy involving pre-oxidation of the nanocomposites through an annealing process at 200 °C in air, which resulted in remarkable sensing stability over a four-week duration. The experimental findings showed that the synthesized SnO_2-based MXene nanocomposite demonstrated improved sensing performance for formaldehyde com-

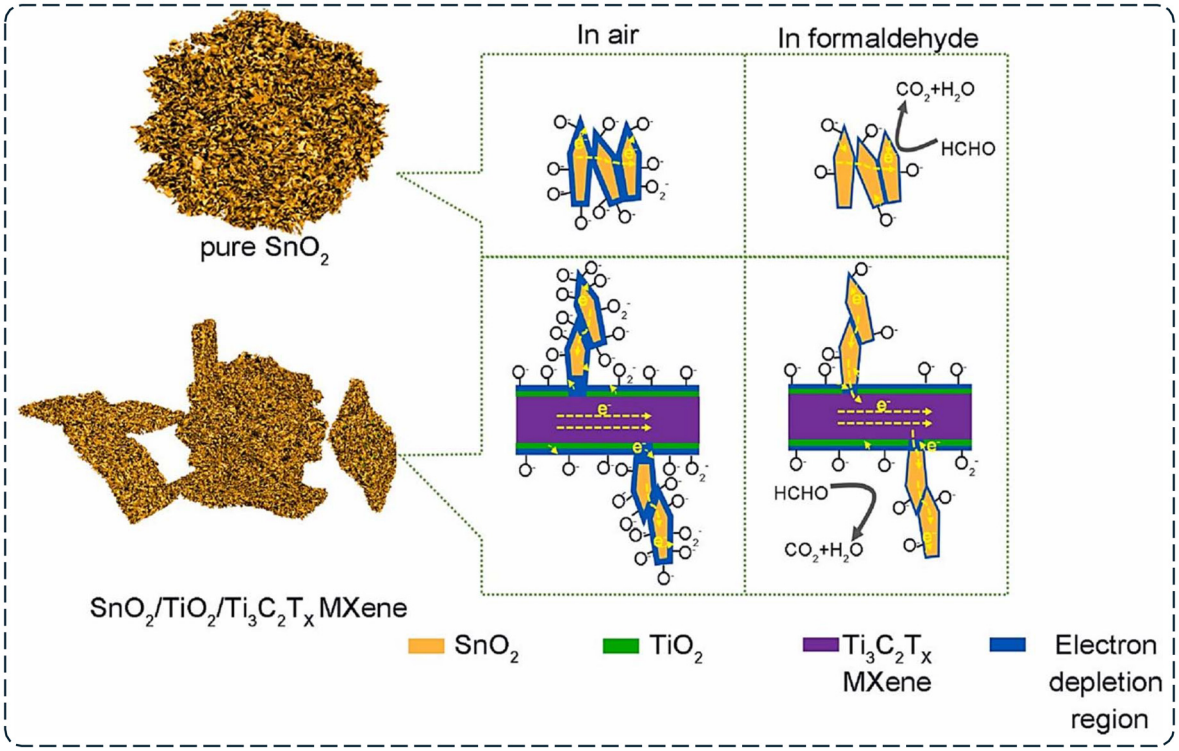

Fig. 5 Schematic of formaldehyde sensing mechanism of pure SnO_2 and $SnO_2/TiO_2/Ti_3C_2T_x$ MXene composite.[119]

pared to pure SnO_2 samples, while the pre-oxidized MXene exhibited minimal response to formaldehyde at 160 °C. The authors attributed the enhancements in sensing and selectivity to the synergistic interaction between SnO_2 nanosheets and $TiO_2/Ti_3C_2T_x$ MXene within the nanocomposites.[162] The sensing mechanism of SnO_2, an n-type metal oxide semiconductor, was explained as the interaction between formaldehyde gas and absorbed oxygen species, resulting in decreased resistance of SnO_2 materials [Fig. 5]. In air, oxygen molecules adsorbed onto the surface of SnO_2 nanosheets captured electrons from the conduction band, leading to the formation of various oxygen species (O_2^-, O^-, and O_2^{2-}). The predominant species in the temperature range of 120–200 °C were O_2^- and O^-. This process created an electron depletion region on the SnO_2 surface, which increased the initial resistance. When formaldehyde gas was introduced, the molecules reacted with the O_2^- and O^- species. In the SnO_2/MXene nanocomposites, pre-oxidizing the $Ti_3C_2T_x$ MXene increased the concentration of oxygen vacancies, providing additional active sites for the adsorption of both oxygen and formaldehyde molecules. As a result, the sensor exhibited more significant changes in resistance in response to formaldehyde exposure.

It is worth noting however, that excessive $Ti_3C_2T_x$ MXene addition resulted in extremely low carrier concentration in the composite and correspondingly high resistance (~700 Mohm for SnO_2/MXene-5 and SnO_2/MXene-10), whereby electrons released from the sensing reaction had to traverse numerous interfaces/boundaries between $TiO_2/Ti_3C_2T_x$ MXene and SnO_2 in the composites. As such, it is understood that careful control of synthesis procedures and composition control is critical in application and scale-up of durable MXene composites, with one proven strategy proven to be through pre-oxidation of MXene framework.

5.2 NH_3 gas sensors

Ammonia gas was identified as one of the most prevalent gases found in household and industrial cleaners, chemical production, refrigeration systems, agricultural products, and fertilizers.[163–168] Furthermore, it is well known that NH_3 detection could serve as a significant biomarker for disease diagnosis through exhaled breath analysis, particularly for conditions such as chronic liver disease, chronic kidney disease, and peptic ulcer symptoms. Additionally, NH_3 has been established as a quality indicator for various food products, including fish, meat, and marine produce freshness in the produce industry.[169,170] Consequently, room temperature detection of NH_3 became crucial for numerous industries and applications. Although NH_3 is also considered a VOC, due to a wider range of applications and subsequent demand for sensing devices, we selected to dedicate a subsection specifically in recent developments of MXene sensors for detection of ammonia.

In gas sensing applications, pristine $Ti_3C_2T_x$ MXene exhibits high selectivity to NH_3 at room temperature, thanks to its surface terminal functionalities, which include O, F, and OH groups. These functionalities enhance active sites for NH_3 molecule adsorption through hydrogen bonding, making $Ti_3C_2T_x$ MXene a promising material for room temperature NH_3 sensing. However, several challenges remain, such as low

sensitivity, prolonged recovery time for pristine $Ti_3C_2T_x$ MXene, and resistance drift following NH_3 exposure.[171,172]

To address these limitations, researchers incorporated additional carbonaceous nanomaterials such as graphene, carbon nanotubes (CNTs), reduced graphene oxide (rGO), and graphene oxide (GO) to enhance NH_3 gas molecule reactions. For instance, MXene/rGO nanocomposite fibers demonstrated improved NH_3 sensing response at room temperature due to increased concentration in the conduction band and activated adsorption sites. Nevertheless, the sensor response remained relatively low (6.8% at 50 ppm of NH_3) with prolonged recovery times exceeding 20 minutes.[173–175] In efforts to further enhance NH_3 sensing properties of MXene-based gas sensors, metal oxides were selected as effective doping materials due to their ability to generate abundant charge carriers. Copper oxide (CuO) and zinc oxide (ZnO) emerged as prominent metal oxides in gas sensing applications, offering advantages such as good electrical conductivity, non- toxicity, high surface activity sites and long-term stability.[176–178]

Seekaew *et al.*[133] reported the synthesis of $Ti_3C_2T_x$ MXene/GO/CuO/ZnO nanocomposites using the hydrothermal method, exploring various weight ratios to determine the optimal combination for enhanced NH_3 sensing at room temperature. The authors demonstrated that the $Ti_3C_2T_x$ MXene/GO/CuO/ZnO gas sensors exhibited superior response and exceptional selectivity toward NH_3 gas under ambient conditions, highlighting the potential of these nanocomposites for room temperature ammonia detection applications. To obtain the composites, the authors added appropriate amounts of $Ti_3C_2T_x$ MXene and graphene oxide (GO) to deionized water and sonication to obtain a homogenous mixture. Separately, CuO and ZnO powders were also mixed in deionized water and sonicated, followed by the two mixture solutions being combined and sonicated again to reach homogeneity. The mixture then underwent a hydrothermal process at 180 °C for 8 h, and dried to obtain the active sensing material [Fig. 2a]. The authors further investigated the selectivity of six different gas sensors based on varying weight ratios of $Ti_3C_2T_x$ MXene/GO/CuO/ZnO nanocomposites. Their study examined the responses of gas sensors to various gases and volatile organic compounds (VOCs) at room temperature, including ammonia (NH_3), formaldehyde (CH_2O), ethanol (C_2H_5OH), methanol (CH_3OH), isopropanol (C_2H_8O), toluene (C_7H_8), and acetone (C_2H_6O), each at a concentration of 200 ppm. As illustrated in Fig. 6a, the results indicated that all gas sensors

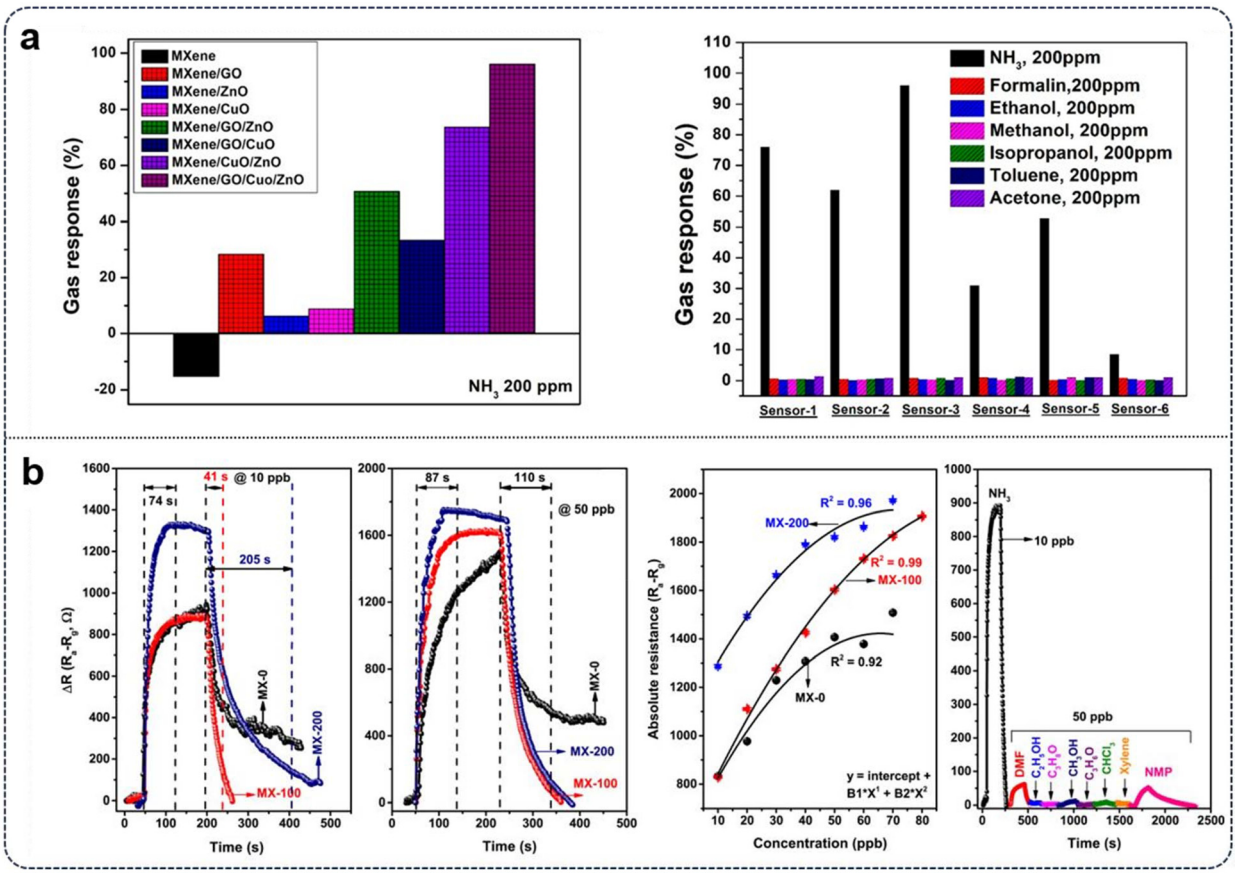

Fig. 6 (a) left: Gas response profile of different compositions of GO, ZnO, and CuO on MXene, right: selectivity histograms of different gases based on different sensor composition rations at room temperature.[90] (b) left: Absolute response profiles at various gas concentrations, including gas selectivity behaviour of MX-100 towards 10 ppb of NH_3, right: comparison of sensor response recovery after exposure to NH_3 on various sensors at 10 ppb and 50 ppb.[136]

exhibited decreased resistance when exposed to NH_2, while showing negligible changes in response to the other VOCs.

Notably, all sensors, particularly Sensor-3, displayed high selectivity for NH_3 compared to the other gases and VOCs, with the $Ti_3C_2T_x$ MXene/GO/CuO/ZnO sensor showing no response to the common oxidizing gas NO_2 at room temperature. In evaluating the $Ti_3C_2T_x$ MXene/GO/CuO/ZnO gas sensors with different weight ratios, researchers found that all configurations exhibited high selectivity and responsiveness to NH_3, with the optimal composition determined to be a 9 : 1 : 5 : 5 weight ratio of $Ti_3C_2T_x$ MXene/GO/CuO/ZnO. Under these optimized conditions, the sensor demonstrated impressive performance characteristics at room temperature, including a 59.9% response to 100 ppm of NH_2, along with rapid response and recovery times of 26 and 25 seconds, respectively. Furthermore, the optimized $Ti_3C_2T_x$ MXene/GO/CuO/ZnO gas sensor exhibited a combination of desirable traits, including high selectivity, significant response magnitude, excellent repeatability, long-term stability, and quick response and recovery times, while maintaining consistent performance across a relative humidity range of 30–70% RH.

The room temperature NH_3-sensing mechanism of the $Ti_3C_2T_x$ MXene/GO/CuO/ZnO nanocomposite was elucidated based on the formation of multiple p–n heterojunctions at the interfaces of its constituent materials. While $Ti_3C_2T_x$ MXene typically exhibited metallic electronic properties, it demonstrated p-type semiconductor behavior in this work, as evidenced by increased resistance upon exposure to electron-donating NH_3. Conversely, GO, CuO, and ZnO displayed n-type conductivity, although their semiconductor properties were noted to be dependent on various factors such as surface functional groups and thermal treatment. The proposed NH_3-sensing mechanism was predicated on forming multiple p–n heterojunctions, facilitated by the varying work functions of the composite materials. As illustrated in Fig. 7, upon exposure to NH_3 gas, the interaction between NH_3 molecules and oxygen species (O_2^-) resulted in electron release to the conduction band of the nanocomposite, leading to a reduction in the electron depletion layer width and the upward band bending. This process decreased the potential barrier at the p–n heterojunction. It promoted the formation of a narrow electron accumulation layer in the n-type components, ultimately causing a decrease in the sensor's resistance at room temperature. The high selectivity of the $Ti_3C_2T_x$ MXene/GO/CuO/ZnO gas sensor towards NH_3 was attributed to the polar nature of NH_3 molecules and the presence of numerous functional groups on the nanocomposite surface, which facilitated stronger hydrogen bonding and enhanced sensing interactions.

In another study, Dogra *et al.*[179] diverged from the common approach of synthesizing metal oxide semiconductor (MOS) and MXene composites separately before combination, instead employing a novel bottom-up methodology to grow MOS directly on the MXene surface during calcination. This technique, which improved the junction contact between TiO_2 and $Ti_3C_2T_x$ MXene, emphasized the critical role of an optimum MO_S/MXene ratio in maximizing sensor response. The researchers developed a facile approach for synthesizing $Ti_3C_2T_x$ MXene and $Ti_3C_2T_x$/TiO_2 composites, wherein TiO_2 was grown through a kinetically controlled calcination process. Their findings revealed that calcination temperature was crucial in determining the overall morphology and sensing performance of $Ti_3C_2T_x$/TiO_2 composites. They also demonstrated that both extremely low and high device resistances were unsuitable for effective conductivity modulation during the sensing process. The enhanced sensing performance was attributed to the formation of heterointerfaces between $Ti_3C_2T_x$ and TiO_2, which facilitated conductivity modulation upon interaction with gas molecules and improved overall sensing capabilities.

Moreover, the response transients revealed varying recovery behaviors among the devices, with MX-0 failing to fully recover its base resistance after gas removal, while MX-100 demonstrated nearly identical resistance changes and recovery to its initial state, with a response time comparable to MX-0. MX-200 exhibited the largest resistance change, albeit with a slightly delayed recovery [Fig. 6b]. At lower concentrations (50 ppb), MX-100 and MX-200 displayed similar recovery times, while MX-0 continued to show delayed recovery, suggesting an interplay between increased resistance due to calcination and various sensing parameters. Among the devices tested, MX-200 demonstrated the largest relative response across the investigated range of ammonia concentrations.

The authors concluded that MXene-based sensing devices exhibited real-time sensitivity to NH_3 under ambient temperature and relative humidity conditions, showcasing their effectiveness in ammonia detection. The devices were exposed to various interfering gases to assess selectivity, a critical factor in sensor performance. The selectivity, influenced by factors such as adsorption and desorption energies of gas molecules, was favourable towards ammonia. This preferential detection was attributed to the composite nature of the sensor ($Ti_3C_2T_x$/TiO_2), with certain crystal planes in TiO_2 being more sensitive to NH_3 adsorption. To validate this selectivity, response transients were acquired for other volatile compounds, including dimethyl formamide, ethanol, isopropyl alcohol, methanol, acetone, chloroform, xylene, and *N*-methyl pyrrolidone, at a concentration of 50 ppb each. The results demonstrated a significantly larger response to ammonia than these interfering gases, confirming the MXene-based devices' selectivity towards reducing ammonia molecules [Fig. 6b].

The reported sensing mechanism agrees with previous studies, wherein TiO_2, an n-type semiconductor with higher electronegativity, exhibited intrinsic oxygen vacancies and, similar to MXene, demonstrated a tendency to absorb atmospheric oxygen on its surface. The adsorbed oxygen is transformed into O_2 after electrons are abstracted from the oxide surface. In the composite system, oxygen adsorption became competitive between the semiconducting oxide and MXene, though in both cases, the adsorbed oxygen converted to O_2^-. TiO_2, with a band gap of 3.2 eV, possessed a work function of 5.1 eV, while the typical work function for MXene ranged from 3.9 eV to 4.8 eV, depending on surface group termination. Assuming a work function of 3.9 eV for MXene, electron flow

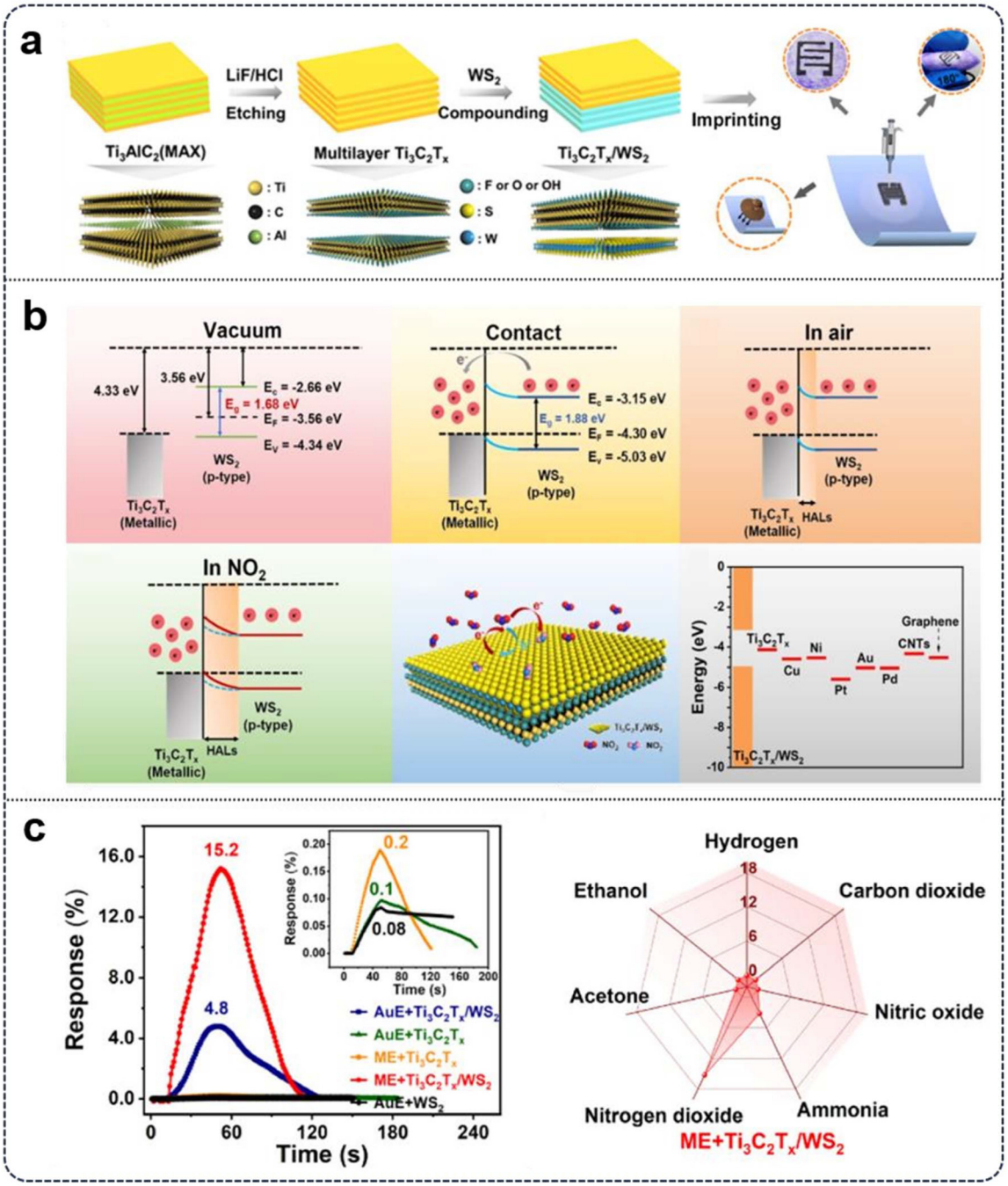

Fig. 7 (a) Schematic of work function and Fermi level positions of $Ti_3C_2T_x$ and p-type WS_2 MXene composite at different gas exposures, illustration of charge transfer process, and work functions of different pristine materials. (b) Synthesis procedure of ME + $To_3C_2T_x/WS_2$ sensor. (c) Sensing value of $Ti_3C_2T_x/WS_2$ sensors on various electrodes.[139]

occurred from MXene to TiO_2 (ϕ = 5.1 eV), forming a depletion layer at the $TiO_2/Ti_3C_2T_x$ composite interface.

The interaction of target gases, whether oxidizing or reducing, modulated the electrical conductivity of the composite. Reducing gases, such as ammonia, donate electrons upon interaction with the sensing surface through two possible mechanisms: interaction with adsorbed O^- ions or OH^- ions associated with processed MXene, both processes resulting in electron release. The released electrons compensated for the depletion layer charges after recombination, enhancing device resistance due to reduced p-type character, which was reflected as an increase in overall device resistance.

5.3 NO_x gas sensors

Among toxic gases, nitrogen dioxide (NO_2) monitoring became particularly crucial due to its association with elevated inci-

dences of respiratory diseases and mortality. Studies demonstrated that prenatal and postnatal exposures to elevated NO_2 levels increased the risk of asthma, hay fever, rhinitis, pneumonia, and eczema in children.[180,181]

A study by Quan *et al.*[182] explored the additional enhancements to the WS_2-based MXene composite by optimization of a flexible electrode material, where three different electrode materials including MXene, graphene, and carbon nanotube, were tested. In a comparative study of flexible printed films, the conductivity of three distinct compositions was evaluated, revealing that the ME composition exhibited superior conductivity, achieving a remarkable 7230 S cm^{-1}. To assess the adhesion properties between the paper substrate, MXene, and $Ti_3C_2T_x/WS_2$ material, they further conducted a simple tape stripping test, concurrently measuring changes in baseline resistance and NO_2 response of the ME + $Ti_3C_2T_x/WS_2$ sensor. Although delamination was observed, the baseline resistance and the response to 200 ppb NO_2 of the flexible $Ti_3C_2T_x/WS_2$ gas sensor remained stable before and after tape stripping, thus demonstrating the excellent adhesion performance of ME and $Ti_3C_2T_x/WS_2$ gas sensing materials when printed on qualitative filter paper. Electrodes were fabricated using Au interdigital electrode (AuE) type gas sensors using $Ti_3C_2T_x$, WS_2, and $Ti_3C_2T_x/WS_2$, while flexible electrode type gas sensors were fabricated using ME + $Ti_3C_2T_x$ and ME + $Ti_3C_2T_x/WS_2$. As depicted in Fig. 8c, the AuE + $Ti_3C_2T_x$ device exhibited higher conduc-

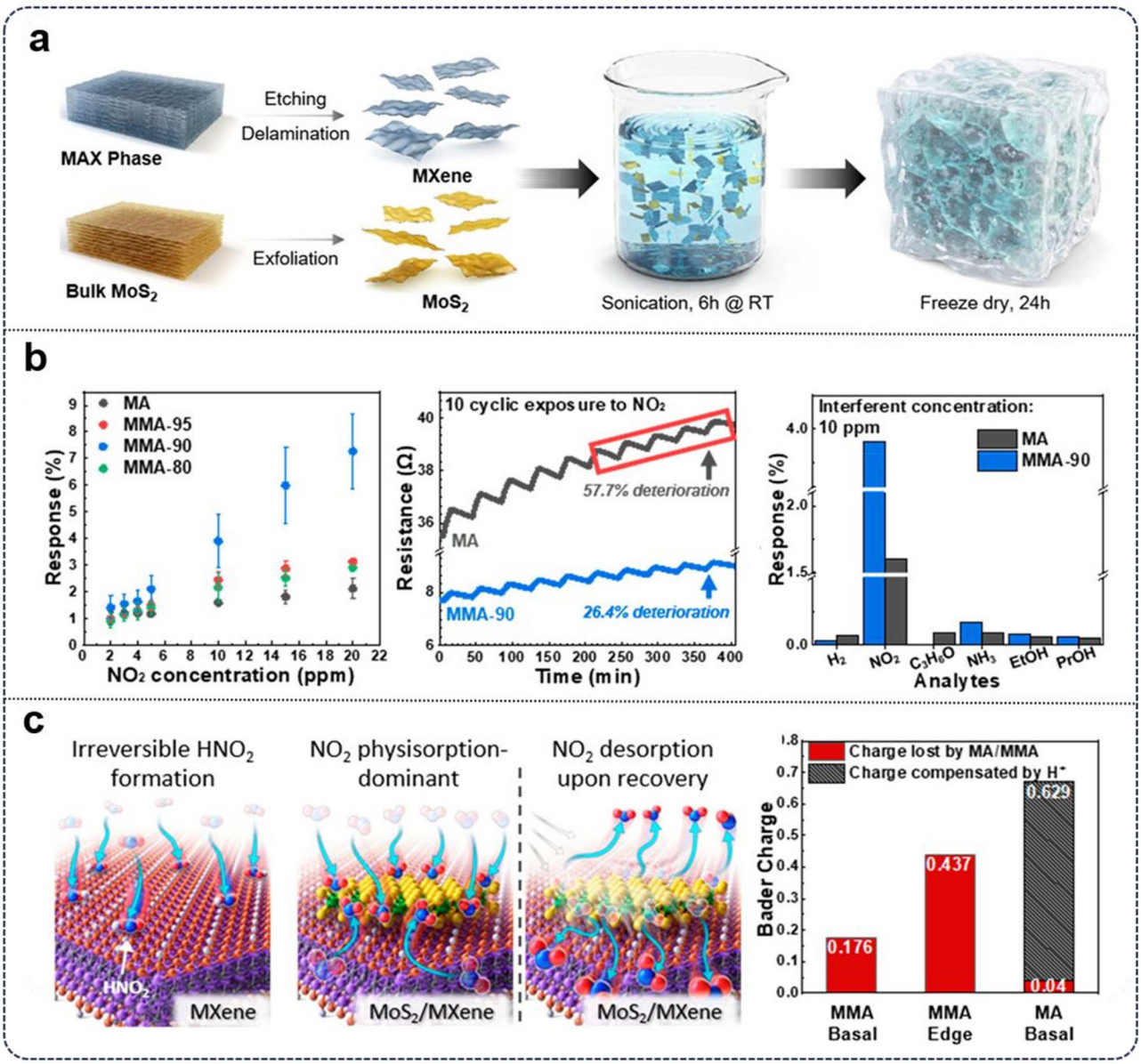

Fig. 8 (a) Fabrication procedure of 3D MoS_2/MXene heterostructure aerogel. (b) Response and recovery profile of MoS_2/MXene towards NO_2, including selectivity profile towards NO_2. (c) Illustration of pristine MXene and MoS_2/MXene, including Bader charge analysis between NO_2 molecules and sensor.[140]

tivity compared to other sensors, however, its NO_2 gas sensing performance was poor, primarily due to the high stacking density of synthetic $Ti_3C_2T_x$. The Schottky-type connection between AuE and WS_2, resulted in incomplete recovery response to 1 ppm NO_2, indicating hampered charge transfer due to mismatched work functions at the AuE-WS_2 interface. The AuE + $Ti_3C_2T_x$/WS_2 sensor exhibited p-type sensing behavior, suggesting NO_2 molecule adsorption inhibited charge carrier transport. Notably, the measured response values showed minimal standard deviations (maximum 0.5%) across various NO_2 concentrations, indicating robust electrode manufacturing stability.

Analysis of the calculated work functions, Fermi level values, and electronic band structures revealed the energy level dynamics between metallic $Ti_3C_2T_x$ and semiconductor WS_2. Upon contact, electron transfer occurred from WS_2 to $Ti_3C_2T_x$ due to work function differences until Fermi level equilibrium was achieved. As illustrated in Fig. 8a, under ambient conditions, oxygen molecules captured electrons from the material, forming chemically adsorbed O_2^- ions on the surface and creating hole accumulation layers (HALs). Upon NO_2 introduction, its higher electron affinity (2.30 eV *versus* 0.44 eV for O_2) facilitated electron transfer, forming NO_3^- and expanding the HALs, thereby reducing resistance. The enhanced NO_2 sensing performance of AuE + $Ti_3C_2T_x$/WS_2 was attributed to both the formation of the $Ti_3C_2T_x$/WS_2 heterojunction layer and the extensive contact areas provided by the 2D/2D heterostructures, which effectively improved carrier transportation.

Continuing the topic of MXene sensing enhancement *via* optimization of electrode morphology and composition, Kim and coworkers[183] presented a synthesis strategy for a three-dimensional (3D) MoS_2/MXene heterostructure aerogel, which was achieved through physical mixing of MoS_2 and MXene nanosheets in deionized water, followed by freeze-drying to form a highly porous hierarchical network, as illustrated in Fig. 8a. Spectroscopic characterization demonstrated that this approach substantially minimized the oxidation degree of the MXene layer while successfully forming van der Waals heterojunctions between MoS_2 and MXene, as confirmed by charge density difference analysis. The fabrication process of the MoS_2/MXene composite aerogel (MMA) began with the synthesis of Ti_3C_2Tx sheets through selective etching of Ti_3AlC_2 in a mixture of LiF and HCl, followed by sonication-induced delamination. MoS_2 nanosheets were prepared using a hydrazine-assisted ball-milling process on bulk MoS_2, whereby the synthesized sheets were then directly assembled into a MoS_2/MXene gel in an aqueous solution. Due to their similar hydrophilicities and negative charges, a stable aqueous MoS_2/$Ti_3C_2T_x$ suspension was readily achieved. To prevent significant oxidation and structural damage, authors employed mild sonication conditions. During freeze-casting, $Ti_3C_2T_x$ sheets interconnected to form a 3D framework, with MoS_2 nanosheets assembling on the MXene framework surfaces. The final MMA composite aerogel was obtained after removing ice crystal templates through freeze-drying, with MMA-X samples where X represented the mass ratio of $Ti_3C_2T_x$ to MoS_2.

The incorporation of the MoS_2 catalytic layer significantly enhanced the resistance variation response toward NO_2 gas. To elucidate the enhancement mechanisms, the researchers investigated charge transfer in two systems: (1) pristine MXene + NO_2 and (2) MXene/MoS_2 + NO_2. Bader charge analysis and charge density calculations revealed decreasing charge transfer from sensing layers to NO_2 in the order of MXene surface (−0.669 eV), MoS_2 edge on MMA (−0.437 eV), and MoS_2 basal plane on MMA (−0.176 eV). Although pristine MXene demonstrated the highest charge transfer, the interaction between NO_2 and MXene surface resulted in hydrogen terminating group withdrawal, leading to charge compensation and reduced overall charge density alteration (0.04 eV). The presence of MoS_2 effectively suppressed HNO_2 formation at both basal plane and edge, resulting in higher charge density alterations in the gas-sensing layer compared to the MXene basal plane. Further analysis showed charge transfer occurred primarily from MoS_2 (−0.447 eV), while MXene's charge density remained relatively stable (0.011 electron gain). The researchers observed that beyond improved response and accelerated NO_2 desorption through transition from chemisorption to physisorption, the MXene's highly selective response toward NO_2 was maintained after MoS_2 decoration. This suggested that the enhancement mechanism was specific to NO_2 gas molecules, as no significant improvements were observed in responses to other interfering gas species (H_2, acetone, NH_3, ethanol, and propanol). This work further demonstrates the multiple avenues of utilization and optimization of MXenes for selective and responsive gas-sensing applications. In addition, it is evident that many previously reported composite sensing materials and frameworks are easily implementable with MXene, raising significant opportunities for rapid development toward a scalable, cost-effective, room temperature gas sensor.

6. Designing MXene heterostructures for gas sensing

It has become evident that a single type of MXene or metal oxide (MO) material proves insufficient for achieving optimal gas sensing response levels. Furthermore, it is also well known the sensing performance of metal oxide materials can be enhanced through integration with conductive materials. When developing MXene hybrid materials for superior sensing performance, several critical factors warrant consideration. The primary requirement involves ensuring the metal oxide material possesses a high specific surface area, as this characteristic facilitates an increased number of available contact points. Additionally, the integration methodology between the metal oxide material and MXene must maintain simplicity. Furthermore, careful regulation of the metal oxide material's work function is essential, as this parameter significantly influences the charge transfer processes occurring at the MO-MXene interface. These requirements make metal oxide

nanoparticles, with their inherent high specific surface area and straightforward fabrication characteristics, particularly suitable candidates for MXene hybrid development.[184]

The resulting composite materials, formed through the combination of MXene and metal oxides, demonstrate distinctive morphological features and properties that result in enhanced sensing capabilities. Moreover, the integration of these heterogeneous structures results in enhanced sensing performance across various volatile organic compounds (VOC) and gaseous molecular species.

Extensive research has been conducted on MXene/metal oxide (hydroxide) materials for gas sensing applications, encompassing investigations of TiO_2, SnO_2, ZnO, WO_3, Fe_2O_3, CuO, In_2O_3, Co_3O_4, $Ni(OH)_2$, $W_{18}O_{49}$, and V_2O_5, among various other compounds as shown in Table 1. Beyond traditional semiconducting metal oxides, researchers have explored a diverse range of materials in developing MXene-metal oxide hybrids for gas sensing applications. Notable examples include $Ti_3C_2T_x$/1D-$K_2W_7O_{22}$ for acetone detection,[185] $Ti_3C_2T_x$/Co_3O_4 for formaldehyde sensing, $Ti_3C_2T_x$/$Ni(OH)_2$ and $Ti_3C_2T_x$/V_2O_5/$CuWO_4$ for NH_3 detection, and $Ti_3C_2T_x$/$Fe_2(MoO_4)_3$ for *n*-butane detection. Nanomaterials of varying dimensionality (0D, 1D, 2D, and 3D) demonstrate unique structural characteristics, resulting in substantially different

Table 1 Gas sensing performance and primary selectivity of MXene heterostructured metal/metal oxide gas sensors

Analyte	MXene composite	Operating temperature (°C)	Analyte concentration (ppm)	Response (%)	Response/recovery time (s s^{-1})	LOD (ppb)	Ref.
Acetone	$Ti_3C_2T_x$/TiO_2	350	2	180	—	20	186
	$Ti_3C_2T_x$/SnO-SnO_2	25	100	12.1	18/9	—	185,187
	$Ti_3C_2T_x$/$W_{18}O_{49}$	300	20	11.6	5.6/6	170	185
	$Ti_3C_2T_x$/(α-/γ-Fe_2O_3)	255	100	215.2	13/8	—	188
	$Ti_3C_2T_x$/α-Fe_2O_3	25	5	16.6	5/5	—	189
	$Ti_3C_2T_x$/$K_2W_7O_{22}$	25	2.86	250	±	—	190
	$Ti_3C_2T_x$/ZnO	320	100	14.4	8/12	—	191
Toluene	$Ti_3C_2T_x$/CuO	250	50	11.4	270/10	320	184
Methane	$Ti_3C_2T_x$/In_2O_3	25	5	29.6	6.5/3.5	—	192
Ethanol	$Ti_3C_2T_x$/TiO_2	25	100	22.47	—	—	193
	$Ti_3C_2T_x$ /TiO_2	25	100	5.90	226/79		194
	$Ti_3C_2T_x$/SnO_2	230	10	500	14/26	—	195
	$Ti_3C_2T_x$/MOF-derived Co_3O_4	200	50	190	50/45	1000	196
	$Ti_3C_2T_x$/MoO_2/MoO_3	25	5	3	46/276	—	197
n-Butane	$Ti_3C_2T_x$/$Fe_2(MoO_4)_3$	120	100	43.1	18/24	—	198
Formaldehyde	$Ti_3C_2T_x$/Co_3O_4	25	10	9.2	83/5	10	199
	$Ti_3C_2T_x$/SnO_2	160	20	10.7	—	—	200
	$Ti_3C_2T_x$/$ZnSnO_3$	25	100	194.7	6.2/5.1	—	201
Hexanal	$Ti_3C_2T_x$/TiO_2	25	10	3.4	293/461	217	202
Triethylamine	$Ti_3C_2T_x$/SnO_2	140	50	33.9	1/1	—	203
	$Ti_3C_2T_x$/WO_3	25	10	277.78	2/3	—	204
Isopropanol	$Ti_3C_2T_x$/TiO_2/MoO_3	25	50	245	100/40	50.45	205
NH_3	$Ti_3C_2T_x$/SnO_2	25	50	40	36/44	4.29	206
	$Ti_3C_2T_x$/SnO	23	10	67	61/119	1000	207
	Ti_2CT_x/TiO_2	25	10	3.1	—	100	208
	$Ti_3C_2T_x$/TiO_2	25	10	3.1	33/277	500	209
	$Ti_3C_2T_x$ /(001)TiO_2	25	30	40.6	10/5	5	209
	$Ti_3C_2T_x$/WO_3	25	1	22.3	119/228		210
	$Ti_3C_2T_x$/α-Fe_2O_3	25	5	18.3	2.5/2	—	211
	$Ti_3C_2T_x$/CuO	25	100	24.8	43/26	—	212
	$Ti_3C_2T_x$/In_2O_3	25	30	63.8	42/209		213
	$Ti_3C_2T_x$/In_2O_3	18	20	100.7	60/300	—	214
	$Ti_3C_2T_x$/MOF-derived In_2O_3	25	5	60.6	3/2	—	215
	$Ti_3C_2T_x$/$Ni(OH)_2$	25	50	11.6	78/-		216
	$Ti_3C_2T_x$/V_2O_5/$CuWO_4$	25	51	53.5	1.6/4	300	217
NO_2	Ti_3C_2/TiO_2	25	5	16.02	—	125	218
	Ti_3C_2/TiO_2	175	100	19.76	150/72	—	219
	$Ti_3C_2T_x$/ZnO	25	100	41.93	34/105		220
	$Ti_3C_2T_x$/ZnO	25	20	367.63	22/10		221
	$Ti_3C_2T_x$/ZnO	25	0.05	81	17/24	0.2	222
	$Ti_3C_2T_x$/ZnO	160	8	3.6	191/254	—	223
	$Ti_3C_2T_x$/ZnO	25	10	25	—	—	224
	$Ti_3C_2T_x$/WO_3	25	0.06	27	162/19.8	—	225
	$Ti_3C_2T_x$/WO_3	25	20	12	96/129	—	226
	$Ti_3C_2T_x$/SnO_2	25	0.03	231	146/102	—	227
	$Ti_3C_2T_x$/SnO_2	150	10	24.8	—	100	228
	$Ti_3C_2T_x$-SnO_2-TiO_2	25	10	32.4	—	100	229
	$Ti_3C_2T_x$/CuO	25	50	56.99	16.6/31.3	—	230
	$Ti_3C_2T_x$/Co_3O_4/Al_2O_3	25	100	40.3	1.3/13.3	10	231
H_2	$Ti_3C_2T_x$/TiO_2	150	500	70	—	—	232

gas-sensitive layers even when utilizing identical metal oxide compositions. Metal oxide nanomaterials, particularly those with 1D structures (such as nanotubes, nanobelts, and nanowires) and 2D configurations (including nanoflakes, nanoplates, and nanosheets), have gained increasing prominence in the development of chemiresistive gas sensors. The selection of nanomaterials with appropriate structural properties has emerged as a crucial factor in optimizing gas sensor parameters, warranting detailed investigation of gas sensors based on these nanomaterials.

SnO_2 represents a highly effective material for gas sensing applications due to its distinctive properties as an inorganic n-type semiconductor exhibiting a wide band gap (3.6 eV to 3.8 eV). The exceptional responsiveness of SnO_2 to various harmful gases and VOCs establishes it as a remarkably promising material for gas sensing applications.[185,195,203] Furthermore, the advancement of SnO_2-MXene gas sensors has garnered significant attention from the research community owing to its potential to enhance both the selectivity and sensitivity of gas sensing devices. In their research, He *et al.*[206] investigated a gas-sensing platform through the integration of 2D MXene heterojunctions with SnO_2 nanoparticles, which were synthesized utilizing a hydrothermal method. The resultant MXene/SnO_2 heterojunctions powder was applied to interdigitated electrodes, and the sensor demonstrated a 40% higher sensitivity to 50 ppm NH_3 compared to a pure MXene sensor when operating at room temperature. ZnO, an n-type semiconductor with a band gap of 3.37 eV is often investigated in for use in gas sensing applications owing to its high response signal to various reducing or oxidizing gases, affordability, and abundance. As a result, reports of ZnO or combinations of, have recently become widespread in selective sensing of NO_2 at room temperature.[220–224] Similar properties have been reported in Tungsten oxide (WO_3) where reports demonstrate high sensitivity and selectivity for NH_3, yielding nearly 16 times higher gain than pristine $Ti_3C_2T_x$.[210] Oxides of iron, copper, and indium have been steadily reported to significantly boost MXene-based sensors' performance with sensitivity towards acetone,[189] toluene,[184] and ammonia,[213,214] respectively. Although significant efforts have been made to enable room temperature sensing *via* incorporation of metal oxide heterojunctions with MXenes as the framework, high operating temperatures, baseline drift, and junction active site degradation or fouling hinder widespread adoption and application of MXene-based sensors.

7. Challenges and future directions

MXene-based heterostructures have shown significant potential in gas sensing applications, offering high sensitivity, selectivity, and operability at room temperature. However, several challenges must be addressed to enable their widespread adoption and practical implementation. This section outlines the key limitations of current MXene-based gas sensors and proposes future research directions to overcome these challenges.

7.1 Stability and oxidation sensitivity

One of the primary limitations of MXenes is their susceptibility to oxidation under ambient conditions, which can degrade sensor performance over time. For example, the oxidation of $Ti_3C_2T_x$ MXene to TiO_2 alters its electrical conductivity and sensing properties, leading to baseline drift and inconsistent responses. Future research should focus on developing passivation strategies—such as protective coatings, controlled surface functionalization, or encapsulation techniques—to enhance long-term stability.

7.2 Selectivity and cross-sensitivity

While MXene-based sensors exhibit excellent sensitivity, achieving high selectivity remains a significant challenge. Many target gases exhibit similar adsorption behaviors on MXene surfaces, leading to cross-sensitivity issues. To improve specificity, the incorporation of selective receptors—such as functionalized polymers or molecularly imprinted layers—could be explored. Additionally, machine learning-based signal processing and pattern recognition techniques may help distinguish between different gas analytes.

7.3 Scalability and integration with flexible electronics

The fabrication of MXene-based sensors at a large scale, while maintaining high reproducibility, remains a challenge. Conventional methods like drop-casting and vacuum filtration often result in inhomogeneous film formation, which affects sensor performance. Future research should focus on scalable synthesis and deposition techniques, such as inkjet printing and roll-to-roll manufacturing, to enable cost-effective, large-area sensor fabrication. Additionally, the integration of MXene-based sensors with flexible and wearable electronics represents an exciting opportunity for real-world applications in biomedical and environmental monitoring.

7.4 Understanding sensing mechanisms and gas adsorption behavior

Although experimental and computational studies have provided valuable insights into the gas-sensing mechanisms of MXenes, a comprehensive understanding of charge transfer dynamics, surface interactions, and gas adsorption kinetics is still lacking. In situ characterization techniques—such as operando X-ray spectroscopy, Raman spectroscopy, and atomic-scale imaging—are essential to elucidate fundamental sensing mechanisms and optimize sensor design.

7.5 Balancing sensitivity and response time

While some sensors (*e.g.*, $Ti_3C_2T_x/WO_3$ for NH_3) demonstrate fast response/recovery times (~1–3 s), others with higher sensitivity (*e.g.*, $Ti_3C_2T_x/In_2O_3$ for NH_3) tend to have longer recovery times (~300 s). This highlights an inherent trade-off between rapid gas adsorption/desorption dynamics and strong gas interactions. Understanding and balancing these trade-offs—depending on the specific application—will be critical for optimizing sensor performance.

8 Summary and outlook

8.1 Summary

In conclusion, MXene-based heterostructures have emerged as highly promising materials for advanced gas sensing applications due to their unique two-dimensional structure, tunable surface chemistry, and excellent conductivity. Since the first synthesis of $Ti_3C_2T_x$ MXene in 2011, substantial progress has been made in enhancing the performance of these materials, particularly for room temperature gas detection. The versatility of MXenes, which allows for various surface functionalities such as –F, –O, and –OH groups, provides a means of tailoring their sensing properties. This has enabled MXenes to detect VOCs like acetone, ethanol, formaldehyde, and gases such as ammonia and nitrogen oxides at extremely low concentrations.

Despite their potential, pristine MXenes face challenges such as baseline drift, low sensitivity at sub- ppm levels, and self-stacking tendencies that hinder gas molecule diffusion. Researchers have developed MXene-based heterostructures to overcome these issues by integrating metal oxides (*e.g.*, SnO_2, ZnO, CuO), polymers, and other 2D materials. These heterostructures introduce new p–n and n–n junctions that modulate charge transfer, leading to improved response times, enhanced stability, and increased gas selectivity. For example, MXene-SnO_2 composites have shown exceptional sensitivity to ammonia at room temperature, benefiting from the formation of depletion layers and an abundance of surface-active sites. Similarly, ZnO/MXene composites have successfully lowered operating temperatures for VOC detection, making them well-suited for low-power, portable devices.

Significant advancements have also been made in MXene synthesis techniques, such as the minimally intensive layer delamination method, which improves control over surface defects and functionalization. This has led to the production of higher-quality MXenes with enhanced gas-sensing properties. Additionally, pre-oxidizing MXenes to improve stability in humid and high-temperature environments has addressed a key challenge, enabling more durable and reliable sensor performance.

8.2 Outlook

However, several challenges remain before MXene-based gas sensors can be fully realized in commercial applications. Scalability in synthesis, long-term operational stability, and performance under varying environmental conditions, such as humidity and temperature, require further optimization. Addressing the self-stacking nature of MXenes, which limits gas diffusion, will also be critical for maximizing sensor performance. Several key challenges in sensing chemistries of MXenes are summarized below:

8.2.1 Durability of MXene materials. MXenes are highly susceptible to oxidation, especially in humid and aqueous environments, which can degrade their electrochemical performance over time. Protecting or passivating MXene sensors without compromising their conductivity or sensitivity remains challenging. Therefore, it is worth considering the location where the sensor is applied and enhancing the material's durability.

8.2.2 Scalability of synthesis. Commercial production of MXene materials (bulk synthesis) can be potentially challenging due to the use of HF to etch MXene. Additional complex heterostructured materials often involve sacrificing several layers of materials and multi-step heat treatment. Lowering the cost, and improving scalability is the next step. Achieving a balance between performance and cost- effectiveness is key for widespread commercial adoption, especially in fields where inexpensive sensors are crucial.

8.2.3 Integration with electric platforms. For MXenes to be commercially viable, they must be compatible with existing sensor manufacturing platforms such as circuit boards. This can be complicated due to their unique properties, like conductivity and hydrophilicity, and they may need specialized processing steps or support materials. Therefore, future studies should examine more of this potential challenge.

Nonetheless, the versatility and room temperature operability of MXene-based heterostructures offer significant potential for applications ranging from environmental monitoring and industrial safety to medical diagnostics and IoT. In-depth studies of the fundamental gas-sensing mechanisms, aided by computational modeling and experimental verification, will be essential for the development of next-generation MXene sensors. Continued progress in this field will pave the way for the large-scale commercialization of MXene-based gas sensors, establishing them as a key technology for future advanced sensing systems.

Data availability

Figures used for this article are available corresponding to the cited articles in the paper. No primary research results, software or code have been included and no new data were generated or analysed as part of this review.

Conflicts of interest

The authors declare no conflict of interest.

Acknowledgements

Y. Z. thank the funding National Natural Science Foundation of China (22250710676), the Natural Science Foundation of Fujian Province (2024J01261), the Educational Research Projects for Young and Middle-aged Teachers in Fujian Province (JZ230002), Fujian Province Super 100 Talents Program, Fujian Province 100 Talents Program, Fujian Province Minjiang Scholar Program. Y. Z. thank Fuzhou University Testing Fund of precious apparatus (2024T010). Y. Z., W. T., and T. Z. would like to acknowledge Fujian province, and the Institute of New Energy Materials

and Engineering, College of Materials Science and Engineering, Fuzhou University. L. Q. thank Natural Sciences and Engineering Research Council of Canada (NSERC) for financial support. L. Q. gratefully thank the *Nanoscale* journal for this invitation article.

References

1 R. Zhang, J. Jiang and W. Wu, *Nanoscale*, 2023, **15**, 3079–3105.
2 S. Dhall, B. R. Mehta, A. K. Tyagi and K. Sood, *Sens. Int.*, 2021, **2**, 100116.
3 M. V. Nikolic, V. Milovanovic, Z. Z. Vasiljevic and Z. Stamenkovic, *Sensors*, 2020, **20**, 6694.
4 G. Hagen, J. Herrmann, X. Zhang, H. Kohler, I. Hartmann and R. Moos, *Sensors*, 2023, **23**, 2930.
5 Y. Yu, Z. Hu, S.-Y. Lien, Y. Yu and P. Gao, *ACS Appl. Mater. Interfaces*, 2022, **14**, 47696–47705.
6 Y. Pan, M. Qin, P. Wang, L. Yang, L. Zhang, C. Yan, C. Zhang and W. Wang, *ACS Sens.*, 2022, **7**, 612–621.
7 X. Li, W. Sun, W. Fu, H. Lv, X. Zu, Y. Guo, D. Gibson and Y.-Q. Fu, *J. Mater. Chem. A*, 2023, **11**, 9216–9238.
8 M. Massetti, F. Jiao, A. J. Ferguson, D. Zhao, K. Wijeratne, A. Würger, J. L. Blackburn, X. Crispin and S. Fabiano, *Chem. Rev.*, 2021, **121**, 12465–12547.
9 J. Wu, G. Yue, W. Chen, Z. Xing, J. Wang, W. R. Wong, Z. Cheng, S. Y. Set, G. Murugan, X. Wang and T. Liu, *ACS Photonics*, 2020, **7**, 2923–2940.
10 C. Love, H. Nazemi, E. El-Masri, K. Ambrose, M. S. Freund and A. Emadi, *Sensors*, 2021, **21**, 3423.
11 M. A. Franco, P. P. Conti, R. S. Andre and D. S. Correa, *Sens. Actuators Rep.*, 2022, **4**, 100100.
12 M. I. A. Asri, M. N. Hasan, M. R. A. Fuaad, Y. M. Yunos and M. S. M. Ali, *IEEE Sens. J.*, 2021, **21**, 18381–18397.
13 S. M. Majhi, A. Mirzaei, S. Navale, H. W. Kim and S. S. Kim, *Nanoscale*, 2021, **13**, 4728–4757.
14 J.-Y. Jeon, B.-C. Kang, Y. T. Byun and T.-J. Ha, *Nanoscale*, 2019, **11**, 1587–1594.
15 Z. U. Abideen, W. U. Arifeen and Y. M. N. D. Y. Bandara, *Nanoscale*, 2024, **16**, 9259–9283.
16 W. Zhang, X. Chen, Y. Chen, H.-Y. Li and H. Liu, *Nanoscale*, 2024, **16**, 12883–12908.
17 J. Li, X. Chen, X. Zhu, Y. Jiang, X. Chang and S. Sun, *Chin. Chem. Lett.*, 2024, **35**, 108286.
18 S. Hong, M. Wu, Y. Hong, Y. Jeong, G. Jung, W. Shin, J. Park, D. Kim, D. Jang and J.-H. Lee, *Sens. Actuators, B*, 2021, **330**, 129240.
19 Y. Jo, Y. K. Jo, J. Lee, H. W. Jang, I. Hwang and D. J. Yoo, *Adv. Mater.*, 2023, **35**, 2206842.
20 H. Zhang, Y. Guo and F. Meng, *Chemosensors*, 2022, **10**, 231.
21 C. Schultealbert, T. Baur, A. Schütze, S. Böttcher and T. Sauerwald, *Sens. Actuators, B*, 2017, **239**, 390–396.
22 J. Zhang, Z. Qin, D. Zeng and C. Xie, *Phys. Chem. Chem. Phys.*, 2017, **19**, 6313–6329.
23 P. Rai, R. Khan, S. Raj, S. M. Majhi, K.-K. Park, Y.-T. Yu, I.-H. Lee and P. K. Sekhar, *Nanoscale*, 2014, **6**, 581–588.
24 S. Sun, *Nanoscale*, 2015, **7**, 10850–10882.
25 N. A. Isaac, I. Pikaar and G. Biskos, *Microchim. Acta*, 2022, **189**, 196.
26 J. B. A. Gomes, J. J. P. C. Rodrigues, R. A. L. Rabêlo, N. Kumar and S. Kozlov, *J. Sens. Actuator Netw.*, 2019, **8**, 57.
27 M. Fleischer and M. Lehmann, *Solid State Gas Sensors-Industrial Application*, Springer Science & Business Media, 2012, vol. 11.
28 A. Tricoli, M. Righettoni and A. Teleki, *Angew. Chem., Int. Ed.*, 2010, **49**, 7632–7659.
29 D. Kohl, *J. Phys. D: Appl. Phys.*, 2001, **34**, R125.
30 S. C. Anjankar and R. Dhavse, *Arabian J. Sci. Eng.*, 2024, **49**, 7013–7028.
31 S. Xue, S. Cao, Z. Huang, D. Yang and G. Zhang, *Materials*, 2021, **14**, 4263.
32 A. Caron, N. Redon, F. Thevenet, B. Hanoune and P. Coddeville, *Build. Environ.*, 2016, **107**, 19–28.
33 G. Korotcenkov, Conventional approaches.
34 M. Grassi, P. Malcovati and A. Baschirotto, *Sensors and Microsystems: AISEM 2009 Proceedings*, Springer, 2010, pp. 25–40.
35 H. J. Lee, U. J. Yang, K. N. Kim, S. Park, K. H. Kil, J. S. Kim, A. M. Wodtke, W. J. Choi, M. H. Kim and J. M. Baik, *Nano Lett.*, 2019, **19**, 4306–4313.
36 D. K. Pattadar and F. P. Zamborini, *Langmuir*, 2019, **35**, 16416–16426.
37 Y. Shimizu and M. Egashira, *MRS Bull.*, 1999, **24**, 18–24.
38 Y. Tang, Y. Zhao and H. Liu, *ACS Sens.*, 2022, **7**, 3582–3597.
39 A. Singh, S. Sikarwar, A. Verma and B. C. Yadav, *Sens. Actuators, A*, 2021, **332**, 113127.
40 S. C. Dhanabalan, B. Dhanabalan, X. Chen, J. S. Ponraj and H. Zhang, *Nanoscale*, 2019, **11**, 3046–3101.
41 J. Zhang, X. Liu, G. Neri and N. Pinna, *Adv. Mater.*, 2016, **28**, 795–831.
42 L. Zhu and W. Zeng, *Sens. Actuators, A*, 2017, **267**, 242–261.
43 Y. Tang, Y. Zhao and H. Liu, *ACS Sens.*, 2022, **7**, 3582–3597.
44 S. G. Chatterjee, S. Chatterjee, A. K. Ray and A. K. Chakraborty, *Sens. Actuators, B*, 2015, **221**, 1170–1181.
45 M. Mittal and A. Kumar, *Sens. Actuators, B*, 2014, **203**, 349–362.
46 S. Basu and P. Bhattacharyya, *Sens. Actuators, B*, 2012, **173**, 1–21.
47 S.-J. Choi and I.-D. Kim, *Electron. Mater. Lett.*, 2018, **14**, 221–260.
48 D. J. Buckley, N. C. G. Black, E. G. Castanon, C. Melios, M. Hardman and O. Kazakova, *2D Mater.*, 2020, **7**, 032002.
49 V. Shukla, J. Warna, N. K. Jena, A. Grigoriev and R. Ahuja, *J. Phys. Chem. C*, 2017, **121**, 26869–26876.
50 Y. Kim, S. Lee, J. Song, K. Y. Ko, W. J. Woo, S. W. Lee, M. Park, H. Lee, Z. Lee and H. Choi, *Adv. Funct. Mater.*, 2020, **30**, 2003360.

51 Y. Kim, S.-K. Kang, N.-C. Oh, H.-D. Lee, S.-M. Lee, J. Park and H. Kim, *ACS Appl. Mater. Interfaces*, 2019, **11**, 38902–38909.
52 S.-J. Choi and I.-D. Kim, *Electron. Mater. Lett.*, 2018, **14**, 221–260.
53 Y. Sun, S. Li, Y. Zhuang, G. Liu, W. Xing and W. Jing, *J. Membr. Sci.*, 2019, **591**, 117350.
54 Y. Du, Z. Yan, W. You, Q. Men, G. Chen, X. Lv, Y. Wu, K. Luo, B. Zhao and J. Zhang, *Adv. Funct. Mater.*, 2023, **33**, 2301449.
55 W. Zeng, X. Ye, Y. Dong, Y. Zhang, C. Sun, T. Zhang, X. Guan and L. Guo, *Coord. Chem. Rev.*, 2024, **508**, 215753.
56 S. Zhang, X. Li, Y. Gao, L. Li, L. Bao and X. Li, *J. Mater. Sci. Technol.*, 2025, **211**, 89–97.
57 S. A. Kazemi, S. A. Ogunkunle, O. Allen, W. Wen, A. W.-C. Liew, S. Yin and Y. Wang, *J. Phys.: Mater.*, 2023, **6**, 035004.
58 J. Li, X. Chen, X. Zhu, Y. Jiang, X. Chang and S. Sun, *Chin. Chem. Lett.*, 2024, **35**, 108286.
59 F. Shahzad, S. A. Zaidi and R. A. Naqvi, *Crit. Rev. Anal. Chem.*, 2022, **52**, 848–864.
60 J. Yang, M. Naguib, M. Ghidiu, L. Pan, J. Gu, J. Nanda, J. Halim, Y. Gogotsi and M. W. Barsoum, *J. Am. Ceram. Soc.*, 2016, **99**, 660–666.
61 M. Han, K. Maleski, C. E. Shuck, Y. Yang, J. T. Glazar, A. C. Foucher, K. Hantanasirisakul, A. Sarycheva, N. C. Frey and S. J. May, *J. Am. Chem. Soc.*, 2020, **142**, 19110–19118.
62 L. Wang, M. Han, C. E. Shuck, X. Wang and Y. Gogotsi, *Nano Energy*, 2021, **88**, 106308.
63 T. L. Tan, H. M. Jin, M. B. Sullivan, B. Anasori and Y. Gogotsi, *ACS Nano*, 2017, **11**, 4407–4418.
64 R. Meshkian, Q. Tao, M. Dahlqvist, J. Lu, L. Hultman and J. Rosen, *Acta Mater.*, 2017, **125**, 476–480.
65 S. K. Nemani, B. Zhang, B. C. Wyatt, Z. D. Hood, S. Manna, R. Khaledialidusti, W. Hong, M. G. Sternberg, S. K. R. S. Sankaranarayanan and B. Anasori, *ACS Nano*, 2021, **15**, 12815–12825.
66 Z. Du, C. Wu, Y. Chen, Z. Cao, R. Hu, Y. Zhang, J. Gu, Y. Cui, H. Chen and Y. Shi, *Adv. Mater.*, 2021, **33**, 2101473.
67 J. Zhou, Q. Tao, B. Ahmed, J. Palisaitis, I. Persson, J. Halim, M. W. Barsoum, P.OÅ. Persson and J. Rosen, *Chem. Mater.*, 2022, **34**, 2098–2106.
68 Q. Li, Y. Li and W. Zeng, *Chemosensors*, 2021, **9**, 225.
69 S. J. Kim, H.-J. Koh, C. E. Ren, O. Kwon, K. Maleski, S.-Y. Cho, B. Anasori, C.-K. Kim, Y.-K. Choi and J. Kim, *ACS Nano*, 2018, **12**, 986–993.
70 E. Lee, A. VahidMohammadi, B. C. Prorok, Y. S. Yoon, M. Beidaghi and D.-J. Kim, *ACS Appl. Mater. Interfaces*, 2017, **9**, 37184–37190.
71 Q. Xia, Y. Fan, S. Li, A. Zhou, N. Shinde and R. S. Mane, *Diamond Relat. Mater.*, 2023, **131**, 109557.
72 H. Zhang, H. He, Y. Huang, S. Pu, Y. Xie, J. Huang, X. Jiang, Y. Wang, S. Wang and H. Peng, *Appl. Surf. Sci.*, 2023, **639**, 158183.
73 M. Naguib, M. W. Barsoum and Y. Gogotsi, *Adv. Mater.*, 2021, **33**, 2103393.
74 Y. Gogotsi and Q. Huang, *ACS Nano*, 2021, **15**, 5775–5780.
75 K. Schwarz, *Crit. Rev. Solid State Mater. Sci.*, 1987, **13**, 211–257.
76 M. W. Barsoum and T. El-Raghy, *J. Am. Ceram. Soc.*, 1996, **79**, 1953–1956.
77 M. W. Barsoum, D. Brodkin and T. El-Raghy, *Scr. Mater.*, 1997, **36**, 535–541.
78 W. Jeitschko, H. Nowotny and F. Benesovsky, *Monatsh. Chem. Verw. Teile Anderer Wiss.*, 1963, **94**, 672–676.
79 M. W. Barsoum, L. Farber, I. Levin, A. Procopio, T. El-Raghy and A. Berner, *J. Am. Ceram. Soc.*, 1999, **82**, 2545–2547.
80 M. W. Barsoum, *Prog. Solid State Chem.*, 2000, **28**, 201–281.
81 M. Naguib, M. Kurtoglu, V. Presser, J. Lu, J. Niu, M. Heon, L. Hultman, Y. Gogotsi and M. W. Barsoum, *Adv. Mater.*, 2011, **23**, 4248–4253.
82 M. Naguib, O. Mashtalir, J. Carle, V. Presser, J. Lu, L. Hultman, Y. Gogotsi and M. W. Barsoum, *ACS Nano*, 2012, **6**, 1322–1331.
83 M. Sokol, V. Natu, S. Kota and M. W. Barsoum, *Trends Chem.*, 2019, **1**, 210–223.
84 E. Lee and D.-J. Kim, *J. Electrochem. Soc.*, 2020, **167**, 037515.
85 X. Liu, T. Ma, N. Pinna and J. Zhang, *Adv. Funct. Mater.*, 2017, **27**, 1702168.
86 Y. Pei, X. Zhang, Z. Hui, J. Zhou, X. Huang, G. Sun and W. Huang, *ACS Nano*, 2021, **15**, 3996–4017.
87 D. Ju, H. Xu, J. Zhang, J. Guo and B. Cao, *Sens. Actuators, B*, 2014, **201**, 444–451.
88 T. Li, W. Zeng, H. Long and Z. Wang, *Sens. Actuators, B*, 2016, **231**, 120–128.
89 Z. Li, N. Wang, Z. Lin, J. Wang, W. Liu, K. Sun, Y. Q. Fu and Z. Wang, *ACS Appl. Mater. Interfaces*, 2016, **8**, 20962–20968.
90 Q. Li, Y. Du, X. Li, G. Lu, W. Wang, Y. Geng, Z. Liang and X. Tian, *Sens. Actuators, B*, 2016, **235**, 39–45.
91 K. Z. Milowska and J. A. Majewski, *J. Phys. Chem. C*, 2014, **118**, 17395–17401.
92 N. M. Nurazzi, N. Abdullah, S. Z. N. Demon, N. A. Halim, A. F. M. Azmi, V. F. Knight and I. S. Mohamad, *Nanotechnol. Rev.*, 2021, **10**, 330–369.
93 V. Kumar, K. Vikrant and K.-H. Kim, *TrAC, Trends Anal. Chem.*, 2019, **121**, 115694.
94 E. Lee, Y. S. Yoon and D.-J. Kim, *ACS Sens.*, 2018, **3**, 2045–2060.
95 R. Kumar, W. Zheng, X. Liu, J. Zhang and M. Kumar, *Adv. Mater. Technol.*, 2020, **5**, 1901062.
96 R. Kumar, N. Goel, M. Hojamberdiev and M. Kumar, *Sens. Actuators, A*, 2020, **303**, 111875.
97 Y.-F. Sun, S.-B. Liu, F.-L. Meng, J.-Y. Liu, Z. Jin, L.-T. Kong and J.-H. Liu, *Sensors*, 2012, **12**, 2610–2631.
98 C. Wang, L. Yin, L. Zhang, D. Xiang and R. Gao, *Sensors*, 2010, **10**, 2088–2106.

99 X. Liu, T. Ma, N. Pinna and J. Zhang, *Adv. Funct. Mater.*, 2017, **27**, 1702168.
100 J. H. Choi, J. Lee, M. Byeon, T. E. Hong, H. Park and C. Y. Lee, *ACS Appl. Nano Mater.*, 2020, **3**, 2257–2265.
101 T. Yang, X. Zhao, Y. He and H. Zhu, *Graphene*, Elsevier, 2018, pp. 157–174.
102 S. S. Varghese, S. Lonkar, K. K. Singh, S. Swaminathan and A. Abdala, *Sens. Actuators, B*, 2015, **218**, 160–183.
103 R. K. Jha, J. V. D'Costa, N. Sakhuja and N. Bhat, *Sens. Actuators, B*, 2019, **297**, 126687.
104 T. Järvinen, G. S. Lorite, J. Peräntie, G. Toth, S. Saarakkala, V. K. Virtanen and K. Kordas, *Nanotechnology*, 2019, **30**, 405501.
105 B. Cho, M. G. Hahm, M. Choi, J. Yoon, A. R. Kim, Y.-J. Lee, S.-G. Park, J.-D. Kwon, C. S. Kim and M. Song, *Sci. Rep.*, 2015, **5**, 8052.
106 E. Lee, A. VahidMohammadi, B. C. Prorok, Y. S. Yoon, M. Beidaghi and D.-J. Kim, *ACS Appl. Mater. Interfaces*, 2017, **9**, 37184–37190.
107 L. Zhang and Y. Yin, *Sens. Actuators, B*, 2013, **185**, 594–601.
108 H. Y. Jeong, D.-S. Lee, H. K. Choi, D. H. Lee, J.-E. Kim, J. Y. Lee, W. J. Lee, S. O. Kim and S.-Y. Choi, *Appl. Phys. Lett.*, 2010, **96**, 213105.
109 M. Aleixandre, M. C. Horrillo, A. Benito and W. K. Maser, in 2018 Spanish Conference on Electron Devices (CDE), IEEE, 2018, pp. 1–4.
110 S.-H. Li, F.-F. Meng, Z. Chu, T. Luo, F.-M. Peng and Z. Jin, *Adv. Condens. Matter Phys.*, 2017, **2017**, 9720973.
111 R. A. Soomro, S. Jawaid, Q. Zhu, Z. Abbas and B. Xu, *Chin. Chem. Lett.*, 2020, **31**, 922–930.
112 C. Verma and K. K. Thakur, *Eur. J. Mol. Clin. Med.*, 2020, **7**, 4429–4450.
113 A. Hermawan, B. Zhang, A. Taufik, Y. Asakura, T. Hasegawa, J. Zhu, P. Shi and S. Yin, *ACS Appl. Nano Mater.*, 2020, **3**, 4755–4766.
114 E. Lee, A. VahidMohammadi, Y. S. Yoon, M. Beidaghi and D.-J. Kim, *ACS Sens.*, 2019, **4**, 1603–1611.
115 K. Deshmukh, T. Kovářík and S. K. K. Pasha, *Coord. Chem. Rev.*, 2020, **424**, 213514.
116 S. J. Kim, H.-J. Koh, C. E. Ren, O. Kwon, K. Maleski, S.-Y. Cho, B. Anasori, C.-K. Kim, Y.-K. Choi and J. Kim, *ACS Nano*, 2018, **12**, 986–993.
117 B. Anasori and Y. Gogotsi, *2D Metal Carbides and Nitrides (MXenes) Structure, Properties and Applications*, 2019, pp. 3–12.
118 H. Huang, R. Jiang, Y. Feng, H. Ouyang, N. Zhou, X. Zhang and Y. Wei, *Nanoscale*, 2020, **12**, 1325–1338.
119 J. Zou, J. Wu, Y. Wang, F. Deng, J. Jiang, Y. Zhang, S. Liu, N. Li, H. Zhang and J. Yu, *Chem. Soc. Rev.*, 2022, **51**, 2972–2990.
120 D. Wang, F. Li, R. Lian, J. Xu, D. Kan, Y. Liu, G. Chen, Y. Gogotsi and Y. Wei, *ACS Nano*, 2019, **13**, 11078–11086.
121 Y. Wei, P. Zhang, R. A. Soomro, Q. Zhu and B. Xu, *Adv. Mater.*, 2021, **33**, 2103148.
122 M. Murugesan, K. R. Nagavenkatesh, P. Devendran, N. Nallamuthu, C. Sambathkumar and M. K. Kumar, *Mater. Sci. Eng., B*, 2024, **309**, 117607.
123 M. Alhabeb, K. Maleski, B. Anasori, P. Lelyukh, L. Clark, S. Sin and Y. Gogotsi, *Chem. Mater.*, 2017, **29**, 7633–7644.
124 J. Halim, S. Kota, M. R. Lukatskaya, M. Naguib, M.-Q. Zhao, E. J. Moon, J. Pitock, J. Nanda, S. J. May, Y. Gogotsi and M. W. Barsoum, *Adv. Funct. Mater.*, 2016, **26**, 3118–3127.
125 M. Alhabeb, K. Maleski, T. S. Mathis, A. Sarycheva, C. B. Hatter, S. Uzun, A. Levitt and Y. Gogotsi, *MXenes*, Jenny Stanford Publishing, 2023, pp. 451–462.
126 M. A. El Saeed, F. A. Deorsola and R. M. Rashad, *Int. J. Refract. Met. Hard Mater.*, 2012, **35**, 127–131.
127 F. Xia, J. Lao, R. Yu, X. Sang, J. Luo, Y. Li and J. Wu, *Nanoscale*, 2019, **11**, 23330–23337.
128 R. A. Soomro, P. Zhang, B. Fan, Y. Wei and B. Xu, *Nano-Micro Lett.*, 2023, **15**, 108.
129 F. Xia, J. Lao, R. Yu, X. Sang, J. Luo, Y. Li and J. Wu, *Nanoscale*, 2019, **11**, 23330–23337.
130 R. A. Soomro, P. Zhang, B. Fan, Y. Wei and B. Xu, *Nano-Micro Lett.*, 2023, **15**, 108.
131 F. Cao, Y. Zhang, H. Wang, K. Khan, A. K. Tareen, W. Qian, H. Zhang and H. Ågren, *Adv. Mater.*, 2022, **34**, 2107554.
132 M. A. Hope, A. C. Forse, K. J. Griffith, M. R. Lukatskaya, M. Ghidiu, Y. Gogotsi and C. P. Grey, *Phys. Chem. Chem. Phys.*, 2016, **18**, 5099–5102.
133 Y. Seekaew, S. Kamlue and C. Wongchoosuk, *ACS Appl. Nano Mater.*, 2023, **6**, 9008–9020.
134 L. C. T. Cao, M.-H. Zhou, P. Opaprakasit, P. Sreearunothai, Y. Nagao, S. Boonruang, H. Fallah, S.-F. Tseng and S.-H. Hsu, *Adv. Mater. Interfaces*, 2023, **10**, 2300166.
135 H. Yu, L. Dai, Y. Liu, Y. Zhou, P. Fan, J. Luo and A. Zhong, *J. Alloys Compd.*, 2023, **962**, 171170.
136 S. M. Aghaei, A. Aasi and B. Panchapakesan, *ACS Omega*, 2021, **6**, 2450–2461.
137 S. J. Kim, H.-J. Koh, C. E. Ren, O. Kwon, K. Maleski, S.-Y. Cho, B. Anasori, C.-K. Kim, Y.-K. Choi, J. Kim, Y. Gogotsi and H.-T. Jung, *ACS Nano*, 2018, **12**, 986–993.
138 L. Qian, S. Durairaj, S. Prins and A. Chen, *Biosens. Bioelectron.*, 2021, **175**, 112836.
139 F. Guo, C. Feng, Z. Zhang, L. Zhang, C. Xu, C. Zhang, S. Lin, H. Wu, B. Zhang, A. Tabusi and Y. Huang, *Sens. Actuators, B*, 2023, **375**, 132885.
140 Z. Wang, F. Wang, A. Hermawan, Y. Asakura, T. Hasegawa, H. Kumagai, H. Kato, M. Kakihana, J. Zhu and S. Yin, *J. Mater. Sci. Technol.*, 2021, **73**, 128–138.
141 P. Song, D. Xiong, W. Jiang, H. Zhang, K. Wu, Y. Xie, Z. Feng, T. Wang, Q. Wang and M. He, *Ionics*, 2023, **29**, 3991–4000.
142 S. Gasso, M. K. Sohal and A. Mahajan, *Sens. Actuators, B*, 2022, **357**, 131427.
143 H. Yu, L. Dai, Y. Liu, Y. Zhou, P. Fan, J. Luo and A. Zhong, *J. Alloys Compd.*, 2023, **962**, 171170.

144 L. Yao, X. Tian, X. Cui, R. Zhao, M. Xiao, B. Wang, X. Xiao and Y. Wang, *Sens. Actuators, B*, 2022, **358**, 131501.
145 A. Marchand, J. Ménard, P. Brochu and S. Haddad, *Environ. Toxicol. Pharmacol.*, 2021, **88**, 103737.
146 T. Fowler, B. Thompson and J. Mueller, *Rem. J.*, 2011, **22**, 9–28.
147 H. Guo, Z. H. Ling, K. Cheung, D. W. Wang, I. J. Simpson and D. R. Blake, *Atmos. Environ.*, 2013, **65**, 80–88.
148 K. Karimi, M. Tabatabaei, I. S. Horváth and R. Kumar, *Biofuel Res. J.*, 2015, **2**, 301–308.
149 B. Sun, Y. Ding, Q. Wang and P. Song, *Sens. Actuators, B*, 2024, **409**, 135541.
150 D. D. Hsu, D. Inman, G. A. Heath, E. J. Wolfrum, M. K. Mann and A. Aden, *Environ. Sci. Technol.*, 2010, **44**, 5289–5297.
151 D. Pimentel, *Nat. Resour. Res.*, 2003, **12**, 127–134.
152 S. K. Lin, *Molecules*, 2001, **6**, 1019–1020.
153 P. C. Badger and J. D. Broder, *HortScience*, 1989, **24**, 227–232.
154 S. Zhang, Y. Ding, Q. Wang and P. Song, *Sens. Actuators, B*, 2023, **393**, 134122.
155 T. Salthammer, S. Mentese and R. Marutzky, *Chem. Rev.*, 2010, **110**, 2536–2572.
156 C. W. F. Yu and J. T. Kim, *Indoor Built Environ.*, 2012, **21**, 137–149.
157 H. Reingruber and L. B. Pontel, *Curr. Opin. Toxicol.*, 2018, **9**, 28–34.
158 H. Reingruber and L. B. Pontel, *Curr. Opin. Toxicol.*, 2018, **9**, 28–34.
159 Z. Li, Q. Zhao, W. Fan and J. Zhan, *Nanoscale*, 2011, **3**, 1646–1652.
160 Z. Deng, Y. Zhang, D. Xu, B. Zi, J. Zeng, Q. Lu, K. Xiong, J. Zhang, J. Zhao and Q. Liu, *ACS Sens.*, 2022, **7**, 2577–2588.
161 S. R. Mishra and M. Ahmaruzzaman, *Nanoscale*, 2022, **14**, 1566–1605.
162 G. Niu, M. Zhang, B. Wu, Y. Zhuang, R. Ramachandran, C. Zhao and F. Wang, *Ceram. Int.*, 2023, **49**, 2583–2590.
163 P. Berwal, S. Kumar and B. Khandelwal, *J. Energy Inst.*, 2021, **99**, 273–298.
164 J. I. van der Vlugt, *Chem. Soc. Rev.*, 2010, **39**, 2302–2322.
165 X. Meng and K. N. Han, *Miner. Process. Extr. Metall. Rev.*, 1996, **16**, 23–61.
166 S. M. McGinn and H. H. Janzen, *Can. J. Soil Sci.*, 1998, **78**, 139–148.
167 D. A. Khudhur, T. A. Abdullah and N. Norazahar, *ACS Chem. Health Saf.*, 2022, **29**, 394–404.
168 Y. Huang, S. C. Lee, K. F. Ho, S. S. H. Ho, N. Cao, Y. Cheng and Y. Gao, *Atmos. Environ.*, 2012, **59**, 224–231.
169 M. P. Diana, W. S. Roekmijati and W. U. Suyud, in E3S Web of Conferences, EDP Sciences, 2018, vol. 73, p. 06003.
170 C. Liu, Y. Qiao, Y. Guo and K. Guo, *Matter*, 2024, **7**, 2673–2675.
171 K. Cheng, X. Tian, S. Yuan, Q. Feng and Y. Wang, *Sensors*, 2024, **24**, 4465.
172 S. Atkare, S. D. Kaushik, S. Jagtap and C. S. Rout, *Dalton Trans.*, 2023, **52**, 13831–13851.
173 Y. Peng and J. Li, *Front. Environ. Sci. Eng.*, 2013, **7**, 403–411.
174 W. Chen, F. Deng, M. Xu, J. Wang, Z. Wei and Y. Wang, *Sens. Actuators, B*, 2018, **273**, 498–504.
175 S. Zhu, H. Sun, X. Liu, J. Zhuang and L. Zhao, *Sci. Rep.*, 2017, **7**, 14773.
176 D. K. Chaudhary, Y. S. Maharjan, S. Shrestha, S. Maharjan, S. P. Shrestha and L. P. Joshi, *J. Phys. Sci.*, 2022, **33**, 97–108.
177 R. K. Bedi and I. Singh, *ACS Appl. Mater. Interfaces*, 2010, **2**, 1361–1368.
178 S. Bhuvaneshwari and N. Gopalakrishnan, *J. Colloid Interface Sci.*, 2016, **480**, 76–84.
179 N. Dogra, S. Gasso, A. Sharma, K. K. Sharma and S. Sharma, *Surf. Interfaces*, 2024, **48**, 104290.
180 A. Faustini, R. Rapp and F. Forastiere, *Eur. Respir. J.*, 2014, **44**, 744–753.
181 R. W. Atkinson, B. K. Butland, H. R. Anderson and R. L. Maynard, *Epidemiology*, 2018, **29**, 460–472.
182 W. Quan, J. Shi, H. Luo, C. Fan, W. Lv, X. Chen, M. Zeng, J. Yang, N. Hu, Y. Su, H. Wei and Z. Yang, *ACS Sens.*, 2023, **8**, 103–113.
183 S. Kim, H. Shin, J. Lee, C. Park, Y. Ahn, H.-J. Cho, S. Yuk, J. Kim, D. Lee and I.-D. Kim, *ACS Nano*, 2023, **17**, 19387–19397.
184 A. Hermawan, B. Zhang, A. Taufik, Y. Asakura, T. Hasegawa, J. Zhu, P. Shi and S. Yin, *ACS Appl. Nano Mater.*, 2020, **3**, 4755–4766.
185 S. Sun, M. Wang, X. Chang, Y. Jiang, D. Zhang, D. Wang, Y. Zhang and Y. Lei, *Sens. Actuators, B*, 2020, **304**, 127274.
186 H. Pazniak, I. A. Plugin, M. J. Loes, T. M. Inerbaev, I. N. Burmistrov, M. Gorshenkov, J. Polcak, A. S. Varezhnikov, M. Sommer and D. V. Kuznetsov, *ACS Appl. Nano Mater.*, 2020, **3**, 3195–3204.
187 Z. Wang, F. Wang, A. Hermawan, Y. Asakura, T. Hasegawa, H. Kumagai, H. Kato, M. Kakihana, J. Zhu and S. Yin, *J. Mater. Sci. Technol.*, 2021, **73**, 128–138.
188 D. Huang, H. Li, Y. Wang, X. Wang, L. Cai, W. Fan, Y. Chen, W. Wang, Y. Song and G. Han, *Chem. Eng. J.*, 2022, **428**, 131377.
189 M. Liu, J. Ji, P. Song, M. Liu and Q. Wang, *Sens. Actuators, B*, 2021, **349**, 130782.
190 O. Ama, M. Sadiq, M. Johnson, Q. Zhang and D. Wang, *Chemosensors*, 2020, **8**, 102.
191 Y. Zhu, Y. Ma, D. Wu and G. Jiang, *Sens. Actuators, A*, 2022, **344**, 113740.
192 M. Liu, Z. Wang, P. Song, Z. Yang and Q. Wang, *Ceram. Int.*, 2021, **47**, 23028–23037.
193 M. Hou, S. Guo, L. Yang, J. Gao, T. Hu, X. Wang and Y. Li, *Ceram. Int.*, 2021, **47**, 7728–7737.
194 Z. Wang, F. Wang, A. Hermawan, J. Zhu and S. Yin, *Funct. Mater. Lett.*, 2022, **15**, 2251007.

195 Z. Shao, Z. Zhao, P. Chen, J. Chen, W. Liu, X. Shen and X. Liu, *Inorg. Nano-Met. Chem.*, 2024, **54**, 898–906.
196 X. Bu, F. Ma, Q. Wu, H. Wu, Y. Yuan, L. Hu, C. Han, X. Wang, W. Liu and X. Li, *Sens. Actuators, B*, 2022, **369**, 132232.
197 S. Zhang, P. Song, Y. Zheng, Y. Ding and Q. Wang, *J. Alloys Compd.*, 2022, **925**, 166663.
198 S. Zou, J. Gao, L. Liu, Z. Lin, P. Fu, S. Wang and Z. Chen, *J. Alloys Compd.*, 2020, **817**, 152785.
199 D. Zhang, Q. Mi, D. Wang and T. Li, *Sens. Actuators, B*, 2021, **339**, 129923.
200 G. Niu, R. Ramachandran, C. Zhao and F. Wang, in 2021 21st International Conference on Solid-State Sensors, Actuators and Microsystems (Transducers), 2021, pp. 831–834.
201 Z. Sima, P. Song, Y. Ding, Z. Lu and Q. Wang, *Appl. Surf. Sci.*, 2022, **598**, 153861.
202 D. Kuang, L. Wang, X. Guo, Y. She, B. Du, C. Liang, W. Qu, X. Sun, Z. Wu, W. Hu and Y. He, *J. Hazard. Mater.*, 2021, **416**, 126171.
203 D. Liang, P. Song, M. Liu and Q. Wang, *Ceram. Int.*, 2022, **48**, 9059–9066.
204 Z. Li, D. Zhang, X. Wang, X. Liu, Y. Yang, C. Du, J. Guo and Y. Zhang, *J. Alloys Compd.*, 2023, **939**, 168730.
205 Y. Yao, Y. Han, M. Zhou, L. Xie, X. Zhao, Z. Wang, N. Barsan and Z. Zhu, *J. Mater. Chem. A*, 2022, **10**, 8283–8292.
206 T. He, W. Liu, T. Lv, M. Ma, Z. Liu, A. Vasiliev and X. Li, *Sens. Actuators, B*, 2021, **329**, 129275.
207 L. Yao, X. Tian, X. Cui, R. Zhao, M. Xiao, B. Wang, X. Xiao and Y. Wang, *Sens. Actuators, B*, 2022, **358**, 131501.
208 H. Tai, Z. Duan, Z. He, X. Li, J. Xu, B. Liu and Y. Jiang, *Sens. Actuators, B*, 2019, **298**, 126874.
209 D. Zhang, S. Yu, X. Wang, J. Huang, W. Pan, J. Zhang, B. E. Meteku and J. Zeng, *J. Hazard. Mater.*, 2022, **423**, 127160.
210 X. Guo, Y. Ding, D. Kuang, Z. Wu, X. Sun, B. Du, C. Liang, Y. Wu, W. Qu, L. Xiong and Y. He, *J. Colloid Interface Sci.*, 2021, **595**, 6–14.
211 M. Liu, J. Ji, P. Song, J. Wang and Q. Wang, *J. Alloys Compd.*, 2022, **898**, 162812.
212 D. Wang, D. Zhang, Y. Yang, Q. Mi, J. Zhang and L. Yu, *ACS Nano*, 2021, **15**, 2911–2919.
213 M. Zhou, Y. Han, Y. Yao, L. Xie, X. Zhao, J. Wang and Z. Zhu, *Ceram. Int.*, 2022, **48**, 6600–6607.
214 Z. Liu, T. He, H. Sun, B. Huang and X. Li, *Sens. Actuators, B*, 2022, **365**, 131918.
215 M. Liu, J. Wang, P. Song, J. Ji and Q. Wang, *Sens. Actuators, B*, 2022, **361**, 131755.
216 D. Kuang, X. Guo, Z. Zhu, Y. Ding, X. Sun, Z. Wu, L. Zhang, Y. Zhou and Y. He, *Ceram. Int.*, 2021, **47**, 19471–19480.
217 F. Ranjbar, S. Hajati, M. Ghaedi, K. Dashtian, H. Naderi and J. Toth, *J. Hazard. Mater.*, 2021, **416**, 126196.
218 T. Yang, L. Gao, W. Wang, J. Kang, G. Zhao, D. Li, W. Chen and H. Zhang, *Nano-Micro Lett.*, 2021, **13**, 63.
219 S. Liu, M. Wang, G. Liu, N. Wan, C. Ge, S. Hussain, H. Meng, M. Wang and G. Qiao, *Appl. Surf. Sci.*, 2021, **567**, 150747.
220 Z. Yang, L. Jiang, J. Wang, F. Liu, J. He, A. Liu, S. Lv, R. You, X. Yan, P. Sun, C. Wang, Y. Duan and G. Lu, *Sens. Actuators, B*, 2021, **326**, 128828.
221 C. Fan, J. Shi, Y. Zhang, W. Quan, X. Chen, J. Yang, M. Zeng, Z. Zhou, Y. Su, H. Wei and Z. Yang, *Nanoscale*, 2022, **14**, 3441–3451.
222 J. Wang, Y. Yang and Y. Xia, *Sens. Actuators, B*, 2022, **353**, 131087.
223 X. Liu, H. Zhang, Y. Song, T. Shen and J. Sun, *Sens. Actuators, B*, 2022, **367**, 132025.
224 S. Gasso, M. K. Sohal and A. Mahajan, *Sens. Actuators, B*, 2022, **357**, 131427.
225 D. Wang, D. Zhang, J. Guo, Y. Hu, Y. Yang, T. Sun, H. Zhang and X. Liu, *Nano Energy*, 2021, **89**, 106410.
226 S. Gasso and A. Mahajan, *ACS Sens.*, 2022, **7**, 2454–2464.
227 S. Gasso, M. K. Sohal and A. Mahajan, *Sens. Actuators, B*, 2022, **357**, 131427.
228 S. Kang, A. Mirzaei, K. Y. Shin, W. Oum, D. J. Yu, S. S. Kim and H. W. Kim, *Sens. Actuators, B*, 2023, **375**, 132882.
229 X. Wu, Y. Gong, B. Yang, Z. Mao, Z. Yan, C. Su, S. Xiong, X. Long and X. Wang, *Appl. Surf. Sci.*, 2022, **581**, 152364.
230 F. Guo, C. Feng, Z. Zhang, L. Zhang, C. Xu, C. Zhang, S. Lin, H. Wu, B. Zhang, A. Tabusi and Y. Huang, *Sens. Actuators, B*, 2023, **375**, 132885.
231 B. Sun, F. Qin, L. Jiang, J. Gao, Z. Liu, J. Wang, Y. Zhang, J. Fan, K. Kan and K. Shi, *Sens. Actuators, B*, 2022, **368**, 132206.
232 S. A. M. Chachuli, M. N. Hamidon, M. Ertugrul, M. S. Mamat, O. Coban, F. N. Tuzluca, Y. O. Yesilbag and N. H. Shamsudin, *J. Alloys Compd.*, 2021, **882**, 160671.